Cell Reports

Fragmentation of tissue-resident macrophages during isolation confounds analysis of single-cell preparations from mouse hematopoietic tissues

Graphical abstract

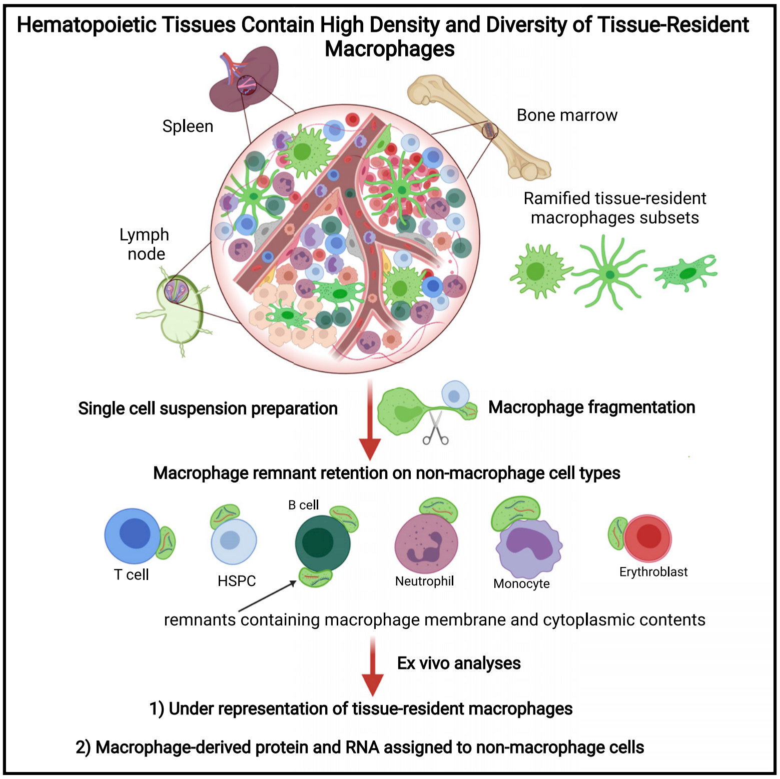

Highlights

- Genuine macrophages are absent from hematopoietic tissue single-cell preparations
- Fragmented remnants of macrophages containing cytoplasm adhere to other cells
- Macrophage remnants convolute hematopoietic tissue flow cytometry analysis
- Remnant-derived macrophage-RNA is misattributed to other cells in RNA-seq data

Authors

Susan M. Millard, Ostyn Heng, Khatora S. Opperman, ..., Liza J. Raggatt, Kim M. Summers, Allison R. Pettit

Correspondence

allison.pettit@mater.uq.edu.au

In brief

Millard et al. demonstrate intact macrophages are absent in hematopoietic tissue single-cell suspensions as they are disrupted during preparation. Macrophage remnants containing membrane and intracellular contents remain attached to other cells within the suspensions. This results in misassignment of macrophage identity and misattribution of macrophage-expressed genes.

Millard et al., 2021, Cell Reports *37*, 110058
November 23, 2021 © 2021 The Author(s).
https://doi.org/10.1016/j.celrep.2021.110058

CellPress

Cell Reports

CellPress
OPEN ACCESS

Article

Fragmentation of tissue-resident macrophages during isolation confounds analysis of single-cell preparations from mouse hematopoietic tissues

Susan M. Millard,[1] Ostyn Heng,[1] Khatora S. Opperman,[2,3] Anuj Sehgal,[1] Katharine M. Irvine,[1] Simranpreet Kaur,[1,4] Cheyenne J. Sandrock,[1] Andy C. Wu,[1,5] Graham W. Magor,[1,6] Lena Batoon,[1] Andrew C. Perkins,[1,6] Jacqueline E. Noll,[2,3] Andrew C.W. Zannettino,[2,3,7] David P. Sester,[5] Jean-Pierre Levesque,[1] David A. Hume,[1] Liza J. Raggatt,[1] Kim M. Summers,[1] and Allison R. Pettit[1,8,*]

[1]Mater Research Institute-The University of Queensland, Translational Research Institute, Woolloongabba, QLD 4102, Australia
[2]Myeloma Research Laboratory, Adelaide Medical School, Faculty of Health and Medical Sciences, University of Adelaide, North Terrace, Adelaide, SA 5005, Australia
[3]South Australian Health and Medical Research Institute, PO Box 11060, Adelaide, SA 5001, Australia
[4]The University of Queensland, UQ Diamantina Institute, Brisbane, QLD 4102, Australia
[5]TRI Flow Cytometry Suite, Translational Research Institute, Woolloongabba, QLD 4102, Australia
[6]Australian Centre for Blood Diseases, Monash University, Melbourne, VIC 3004, Australia
[7]Central Adelaide Local Health Network, Adelaide, SA 5001, Australia
[8]Lead contact
*Correspondence: allison.pettit@mater.uq.edu.au

https://doi.org/10.1016/j.celrep.2021.110058

SUMMARY

Mouse hematopoietic tissues contain abundant tissue-resident macrophages that support immunity, hematopoiesis, and bone homeostasis. A systematic strategy to characterize macrophage subsets in mouse bone marrow (BM), spleen, and lymph node unexpectedly reveals that macrophage surface marker staining emanates from membrane-bound subcellular remnants associated with unrelated cells. Intact macrophages are not present within these cell preparations. The macrophage remnant binding profile reflects interactions between macrophages and other cell types *in vivo*. Depletion of $CD169^+$ macrophages *in vivo* eliminates $F4/80^+$ remnant attachment. Remnant-restricted macrophage-specific membrane markers, cytoplasmic fluorescent reporters, and mRNA are all detected in non-macrophage cells including isolated stem and progenitor cells. Analysis of RNA sequencing (RNA-seq) data, including publicly available datasets, indicates that macrophage fragmentation is a general phenomenon that confounds bulk and single-cell analysis of disaggregated hematopoietic tissues. Hematopoietic tissue macrophage fragmentation undermines the accuracy of macrophage *ex vivo* molecular profiling and creates opportunity for misattribution of macrophage-expressed genes to non-macrophage cells.

INTRODUCTION

Tissues contain abundant resident macrophages that contribute to tissue development, homeostasis, regeneration, and pathology. Within tissues, sub-populations of resident macrophages are defined based upon location and surface markers (Blériot et al., 2020; Hume et al., 2019). Organs that have pleotropic function, like hematopoietic tissues, contain more than one tissue-resident macrophage population, each with distinct functional contributions to specific biological events. Spleen contains macrophage populations with distinct cell-surface marker profiles, including red pulp macrophages integral in phagocytic clearance of erythrocytes and iron recycling, tingible body macrophages responsible for clearance of apoptotic germinal center B cells, metallophilic, and other marginal zone macrophages, contributing to blood filtration and capturing and delivering antigens to either white pulp dendritic cells or marginal zone B cells, respectively (den Haan and Kraal, 2012; Lewis et al., 2019). Similarly, bone and bone marrow (BM) contain abundant resident macrophages that have been subdivided into osteal macrophages (Chang et al., 2008) and those associated with erythroblastic islands (Tay et al., 2020; Yeo et al., 2019) and hematopoietic stem cell (HSC) niches (Chow et al., 2011; Winkler et al., 2010). BM also contains osteoclasts, monocytes, and myeloid progenitors, all of which share surface markers with macrophages.

The resident macrophage populations in many tissues have been isolated and profiled by *ex vivo* analyses including RNA sequencing (RNA-seq) (Summers et al., 2020). However, macrophage yields are often low compared to their abundance *in situ*, and it is unclear whether the full diversity of macrophage phenotypes present *in vivo* have been comprehensively sampled. Mass cytometry analysis across eight murine tissues, including spleen and BM, identified only four resident macrophage

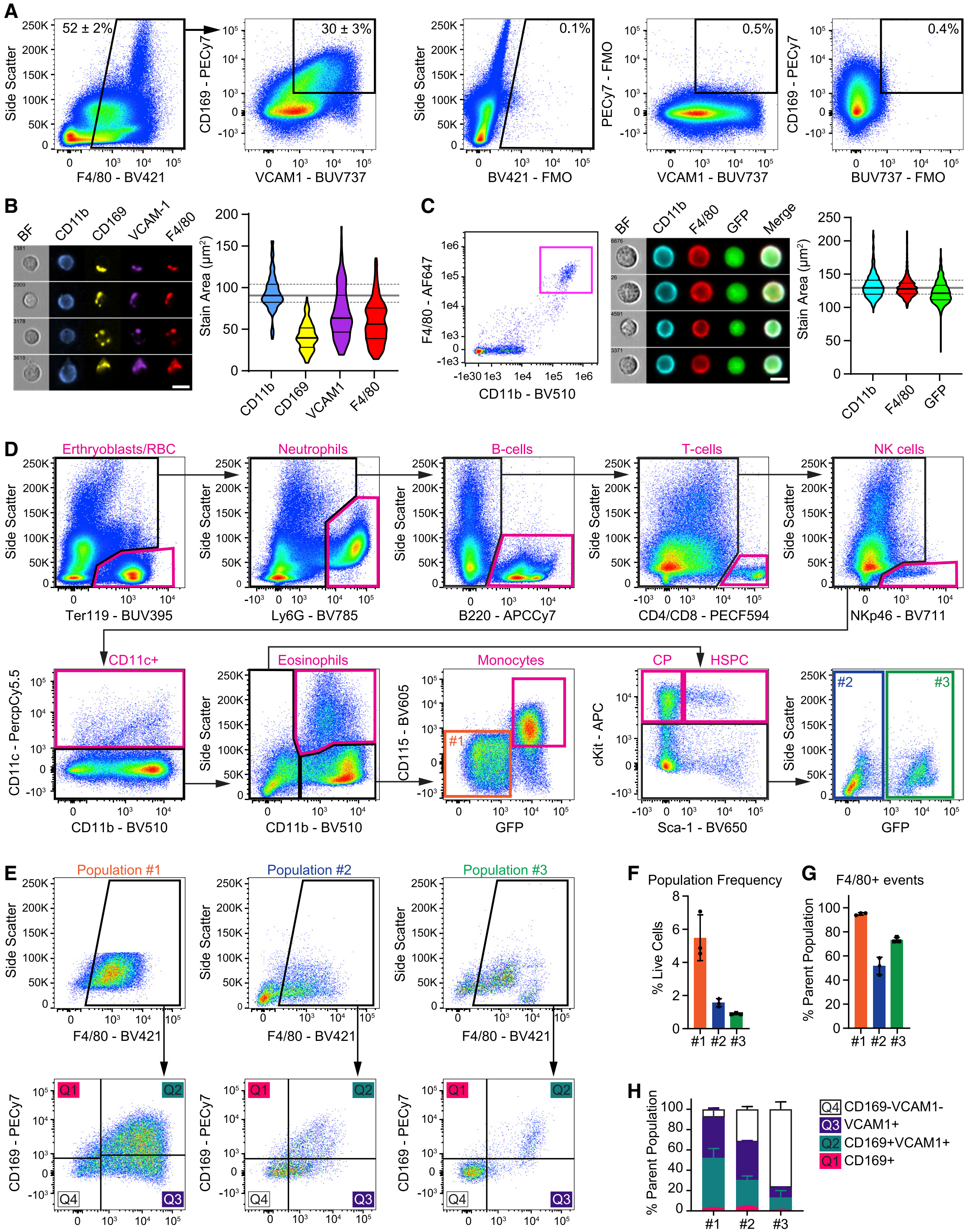

Figure 1. Intact tissue-resident macrophages are not readily identified in bone marrow (BM) cell suspensions

(A) Flow cytometry on live single-cell events demonstrating a substantial F4/80$^+$ BM population, with a subset also staining for CD169 and VCAM-1. This marker profile is consistent with BM resident macrophage identity. Fluorescence minus one (FMO) controls are provided to validate the gates.

(B) Imaging flow cytometry on positively selected CD11b$^+$F4/80$^+$CD169$^+$VCAM-1$^+$ putative macrophage population. Representative images demonstrate punctate CD169, VCAM-1, and F4/80 staining was coincident and contrasted with the cell-surface expression of CD11b. Scale bar, 10 µm. Violin plots of stain area for each marker are included with median and 25th/75th percentiles displayed (n = 142 cells).

(legend continued on next page)

populations. None of these were substantially represented in the BM, where the sum of all macrophage clusters was <1% of the myeloid compartment (Becher et al., 2014). Similarly, a high throughput, low coverage single-cell RNA-seq (scRNA-seq) study designed to profile all BM resident cell types did not identify a single resident macrophage population (Baccin et al., 2020), an outcome that clearly divorces single-cell analysis from known tissue biology. Interestingly, Baccin et al. (2020) specifically comment on a lack of coverage of other cell types, including osteoclasts and mature megakaryocytes, but not the lack of macrophages within their dataset. In addition, high coverage scRNA-seq of over 40,000 cells across 20 mouse organs to generate a transcriptomic atlas of biology demonstrated poor alignment between manual macrophage annotation and unbiased whole-transcriptome-based clustering (Tabula Muris Consortium et al., 2018).

Conventional macrophage gating strategies in naive mouse tissues indicate that macrophages comprise just 0.7% and 1.3% of hematopoietic ($CD45^+$) cells isolated from BM and spleen, respectively (Cossarizza et al., 2019). These proportions are inconsistent with the abundance of resident macrophages (positive for surface markers F4/80 and CSF1R; $F4/80^+CSF1R^+$) in these and other tissues assessed by *in situ* techniques (Grabert et al., 2020; Kaur et al., 2021; Sasmono et al., 2003). An estimate that tissue-resident macrophages constitute 10% to 15% of total cells in tissues is supported by indirect evidence that macrophages contribute around 10% of total mRNA in most organs in the mouse (Summers and Hume, 2017). Using a positive selection macrophage marker profile (*Csf1r*-EGFP $reporter^+F4/80^+VCAM\text{-}1^+$ coupled with validation using CD169 [Siglec1], ER-HR3, MerTK, and/or TIM4 [Kaur et al., 2018]), we improved the efficiency of conventional flow cytometry gating of BM resident macrophages (3.8% of total BM). However, the yield remained low compared to *in situ* quantification of $F4/80^+$ cells (15% of BM area; Kaur et al., 2021), and clear sub-populations reflecting BM macrophage functional diversity were not evident. The absence of a clear $CD169^+$ macrophage population in spleen single-cell preparation and previous studies analyzing cells isolated from lymph node (Gray et al., 2012) or liver (Lynch et al., 2018) suggest that tissue-resident macrophages can be structurally compromised during tissue disruption/digestion. Herein, we delved deeper into *ex vivo* quantification and characterization of hematopoietic tissue-resident macrophages. Our results unexpectedly revealed that macrophages are structurally compromised during processing to obtain single-cell suspensions, resulting in cell artifacts that have clear implications for tissue-resident macrophage molecular profiling and fidelity of *ex vivo* cell analyses of these tissues.

RESULTS

Positive and negative selection strategies to enrich for putative resident macrophages in hematopoietic tissues

By conventional flow cytometry, there are many single-cell events within BM that express the pan-monocyte-macrophage marker F4/80 (Figure 1A). Approximately one third of these express the restricted tissue-resident macrophage marker CD169 and the maturation marker VCAM-1 (Figure 1A). Similar gating strategies, with or without negative selection for mature lymphocyte markers, are commonly used to identify BM and other tissue-resident macrophages. However, imaging flow cytometry analysis of $F4/80^+CD169^+VCAM\text{-}1^+$ events in BM showed that while the staining pattern of the pan-myeloid marker CD11b was uniformly distributed across the cell membrane, the staining pattern of macrophage markers was punctate (Figure 1B). Each of the macrophage markers used showed overlapping distribution and often protruded beyond the cell boundaries apparent in the bright field image. To quantify this anomalous marker distribution, we plotted the stain area of these markers for all events within this gate. The stain area for macrophage markers was significantly smaller, with a broader interquartile range, than the stain area for CD11b that represents the expected stain area for a cell-surface marker (Figure 1B). In gated $CD11b^+CD115^+F4/80^+$ monocytes, F4/80 distribution and stain area are consistent with cell-surface expression (data not shown). Similarly, imaging flow cytometry analysis of thioglycollate-elicited peritoneal lavage cells isolated from *Csf1r*-EGFP reporter mice (Sasmono et al., 2003) confirmed that macrophages in this fluid have cell-surface distribution of CD11b and F4/80 as well as cytoplasmic distribution of EGFP (Figure 1C). These results suggested that BM resident macrophages were not captured using the positive gating strategy.

Consequently, a systematic negative selection strategy on gated single-cell events was used to identify resident macrophage subsets in hematopoietic organs. Cells isolated from *Csf1r*-EGFP reporter mice were stained with an antibody panel designed to delineate mature hematopoietic cell lineages and broad progenitor cell subsets (Figure 1D; Figure S1). Defined non-macrophage cell populations (Figure 1D, specified in magenta text) accounted for 91% ± 1% of live cell singlets in BM, 97% ± 2% in spleen, and 98% ± 0.4% in lymph node (Table

(C) Imaging flow cytometry on positively selected $CD11b^+F4/80^{hi}$ thioglycollate-elicited peritoneal macrophages (magenta gate) isolated from *Csf1r*-EGFP reporter mice. Representative images of demonstrate cell-surface distribution of CD11b and F4/80 and intracellular distribution of GFP. Violin plots of stain area for each marker with median and 25th/75th percentiles displayed are included (n = 573 cells).

(D) Flow cytometry gating strategy employed on single-cell events to identify and exclude defined non-macrophage hematopoietic populations in BM from *Csf1r*-EGFP reporter mice. Excluded cell populations are labeled in magenta and remaining putative macrophage populations labeled in orange (1), blue (2), and green (3). Application of this gating strategy to spleen (SPLN), lymph node (LN), and peripheral blood is shown in Figure S1. Cell frequency data for each population in each tissue is summarized in Table S1.

(E) Gating strategy employed to examine macrophage-marker expression on putative macrophage populations in BM.

(F) Frequency of putative macrophage populations in BM.

(G) Frequency of $F4/80^+$ staining on putative macrophage populations in BM. These data are summarized in Table S2.

(H) Subsetting of $F4/80^+$ events based on CD169 and VCAM-1 staining on each of the putative macrophage populations. For (F), (G), and (H), data are represented as mean ± SD; n = 3.

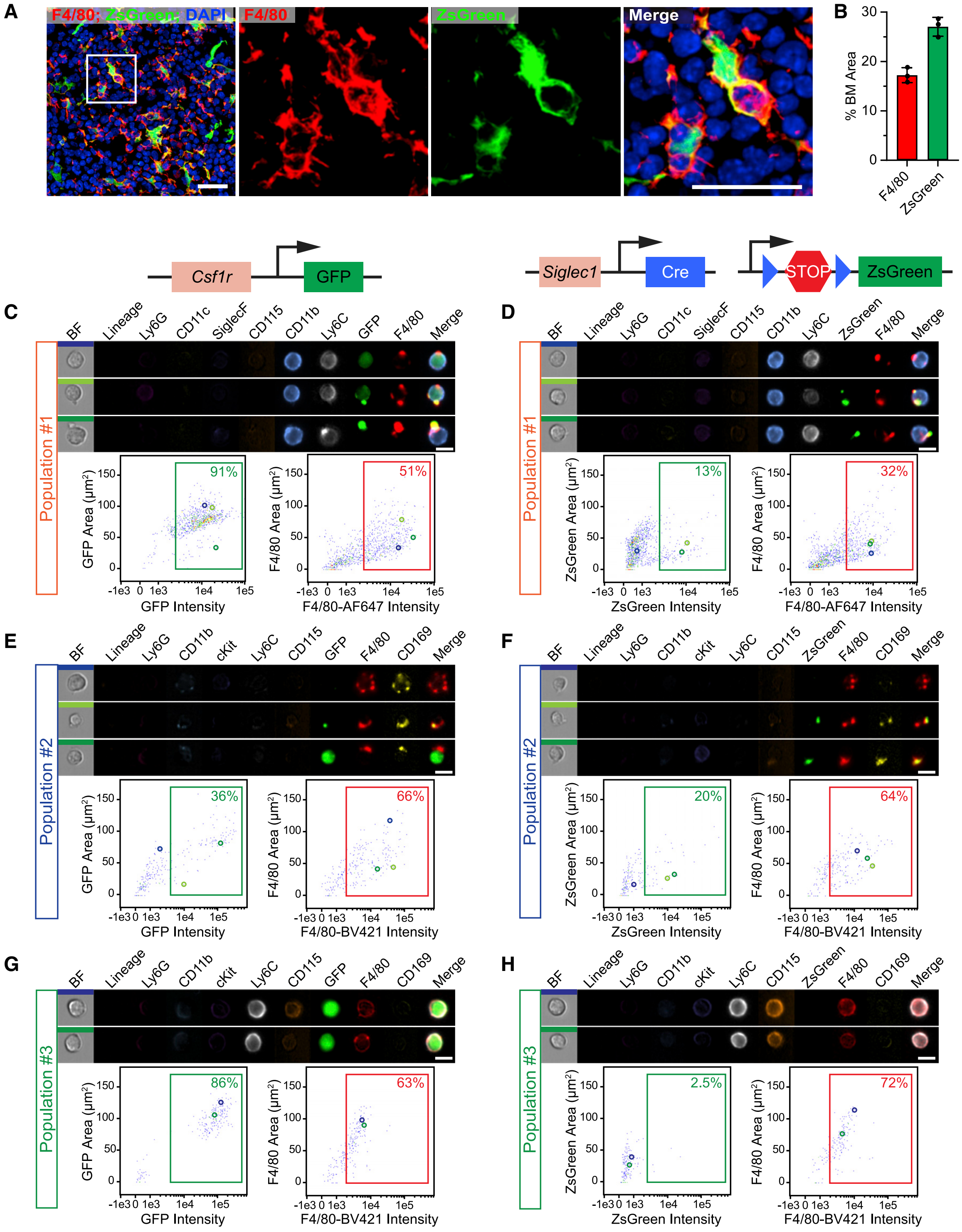

Figure 2. Macrophage markers on BM cells in suspension are not indicative of intact macrophages

(A) Co-expression of the cell-surface pan-macrophage marker F4/80 and cytoplasmic ZsGreen reporter in BM from *Siglec1*^{Cre};*R26*^{ZsGreen} reporter mice. Scale bars, 25 µm.

(B) Estimation of macrophage frequency in BM by quantification of stain area of the cell-surface marker, F4/80, and the cytoplasmic marker, ZsGreen, in bone cryosections as represented in (A). Data are represented as mean ± SD; n = 3.

(legend continued on next page)

S1). Following exclusion of lineage markers (Ter119, Ly6G, B220, CD4/CD8, NKp46, and CD11c), the remaining cells were sub-gated into three populations: (1) lineage$^-$CD11b$^+$ Ly6G$^-$CD115$^{-/lo}$EGFP$^{-/lo}$, (2) lineage$^-$CD11b$^-$Kit$^{-/lo}$EGFP$^-$, and (3) lineage$^-$CD11b$^-$Kit$^{-/lo}$EGFP$^+$ (Figure 1D, final 3 panels). Subsets of populations 1 through 3 were stained for F4/80, VCAM-1, and CD169 (Figures 1E–1H). The frequency of F4/80$^+$ events within these populations was typically highest in population 1 but also varied between hematopoietic/lymphoid tissues (Table S2). Based on this, the population most likely representing hematopoietic macrophages is population 1, equating to 5.5% ± 1.4% of total BM cells. This remains lower than the apparent abundance of F4/80$^+$ staining distribution observed in BM *in situ* (Figures 2A and 2B). Moreover, the population 1 marker profile of CD11b$^+$Ly6G$^-$CD115$^-$ resembles that of neutrophil precursors (Kim et al., 2017; Zhu et al., 2018).

Hematopoietic tissue single-cell preparations do not contain intact resident macrophages

Based upon these inconclusive observations, we used imaging flow cytometry to scrutinize the distribution of the cell-surface markers and reporter molecules in these populations. *Csf1r*-EGFP reporter expression was confirmed in B cells, neutrophils, and monocytes (Figures S2A and S2B; Sasmono et al., 2003). SiglecF$^+$ eosinophils showed variable expression of the *Csf1r*-EGFP reporter but no cell-surface CD115/CSF1R (Figures S2A and S2B; Hawley et al., 2018). Cell-surface F4/80 expression was observed on monocytes and eosinophils (Fukushima et al., 2010; Hamann et al., 2007). We also employed a *Siglec1*^{Cre};*R26*^{ZsGreen} conditional reporter for improved specificity for BM resident macrophages. In the BM, *in situ* imaging showed coincident expression of ZsGreen in F4/80$^+$ ramified macrophages (Figures 2A and 2B). Imaging flow cytometry confirmed that the ZsGreen reporter was absent from erythroblasts, B cells and T cells (i.e., lineage), neutrophils, eosinophils, and monocytes (Figure S2C).

Figures 2C–2H shows imaging flow cytometry of the three identified putative BM macrophage populations from *Csf1r*-EGFP or *Siglec1*^{Cre};*R26*^{ZsGreen} mice (gating strategies: Figures S2A and S2D). In *Csf1r*-EGFP mice, population 1 was 91% EGFP$^+$, with the majority of gated events having cytoplasmic distribution consistent with endogenous EGFP expression (Figure 2C; median EGFP stain area = 76 μm^2/cell). The same cells expressed surface CD11b and Ly6C, consistent with myeloid lineage identity. However, F4/80 staining was polarized/punctate, being restricted to one or more foci associated with the imaged cell (Figure 2C; median F4/80 stain area = 41 μm^2/cell). In some instances, EGFP expression colocalized with the intense foci of F4/80 expression (Figure 2C). In contrast, few cells in this same population isolated from *Siglec1*^{Cre};*R26*^{ZsGreen} mice expressed cytoplasmic ZsGreen (Figure 2D). When ZsGreen was present, it was coincident with foci of F4/80 staining, not distributed throughout the cytoplasm of the imaged cell (Figure 2D).

Among population 2, fewer events expressed *Csf1r*-EGFP reporter than F4/80, and when present, EGFP distribution was often coincident with F4/80 (Figure 2E). In this population, *Siglec1*^{Cre};*R26*^{ZsGreen} reporter was again consistently coincident with focal F4/80 staining (Figure 2F). Population 3 cells had high EGFP expression in *Csf1r*-EGFP mice, with the staining area indicative of large cells (Figure 2G; median GFP stain area = 98 μm^2). They frequently expressed surface CD115 and also displayed uniform cell-surface F4/80 staining (Figures 2G and 2H). However, neither cell-surface CD169 nor ZsGreen were detected, indicating this minor *ex vivo* population does not represent the dominant F4/80$^+$ZsGreen$^+$ macrophages observed in bone tissue sections (Figure 2A).

In summary, the putative macrophage populations represent immature myeloid cells, not tissue-resident macrophages. While a distinct population of BM macrophages cannot be identified within hematopoietic tissue single cell suspensions, events that would reasonably be interpreted as tissue-resident macrophages using traditional flow cytometry were shown to be non-macrophage cells cloaked with fragmented cell remnants likely donated by ramified macrophages disrupted during single-cell preparation. These observations were not specific to one anti-F4/80 antibody clone or specific fluorophore artifact (Figure S3). Importantly, the putative macrophage remnants retain cytoplasmic reporter proteins (EGFP, ZsGreen).

Fragmented resident macrophage remnants are found on many distinct cell types and have tissue-specific distribution

The presence of macrophage remnants was not restricted to immature myeloid populations enriched by negative selection. Figure 3 shows that macrophage remnants were associated with mature hematopoietic lineage cells, including erythroblasts, B cells, T cells, and neutrophils, in both BM (Figure 3A; gated as outlined in Figures S4A and S4B) and spleen (Figure 3B; gated as outlined in Figures S4C and S4D). With the exception of monocytes, which displayed endogenous-cell-surface F4/80 expression, the F4/80 stain area for each cell type was significantly lower than the stain area of the defining cell-surface marker (Figures 3C and 3D).

To visualize the extent to which tissue-resident macrophage remnants were present across hematopoietic lineages in single-cell suspensions, conventional flow cytometry data from BM, spleen, lymph node, and blood (Figure 1A; Figure S1) were pooled and dimensionality reduction (t-distributed stochastic neighbor embedding [t-SNE]) applied based on lineage

---

(C and D) Representative images from putative macrophage population 1 in BM from *Csf1r*-EGFP (C) and *Siglec1*^{Cre};*R26*^{ZsGreen} (D) mice. The gating strategy is outlined in Figure S2A. The colored bars on the brightfield (BF) images correspond to the colored circles on matched plots of stain area against stain intensity, placing the visualized images in the context of the dataset. Scale bar, 10 μm.

(E and F) Representative images from putative macrophage population 2 in BM from *Csf1r*-EGFP (E) and *Siglec1*^{Cre};*R26*^{ZsGreen} (F) mice. The gating strategy is outlined in Figure S2D. Scale bar, 10 μm.

(G and H) Representative images from putative macrophage population 3 in BM from *Csf1r*-EGFP (G) and *Siglec1*^{Cre};*R26*^{ZsGreen} (H) mice. The gating strategy is outlined in Figure S2D. Scale bar, 10 μm.

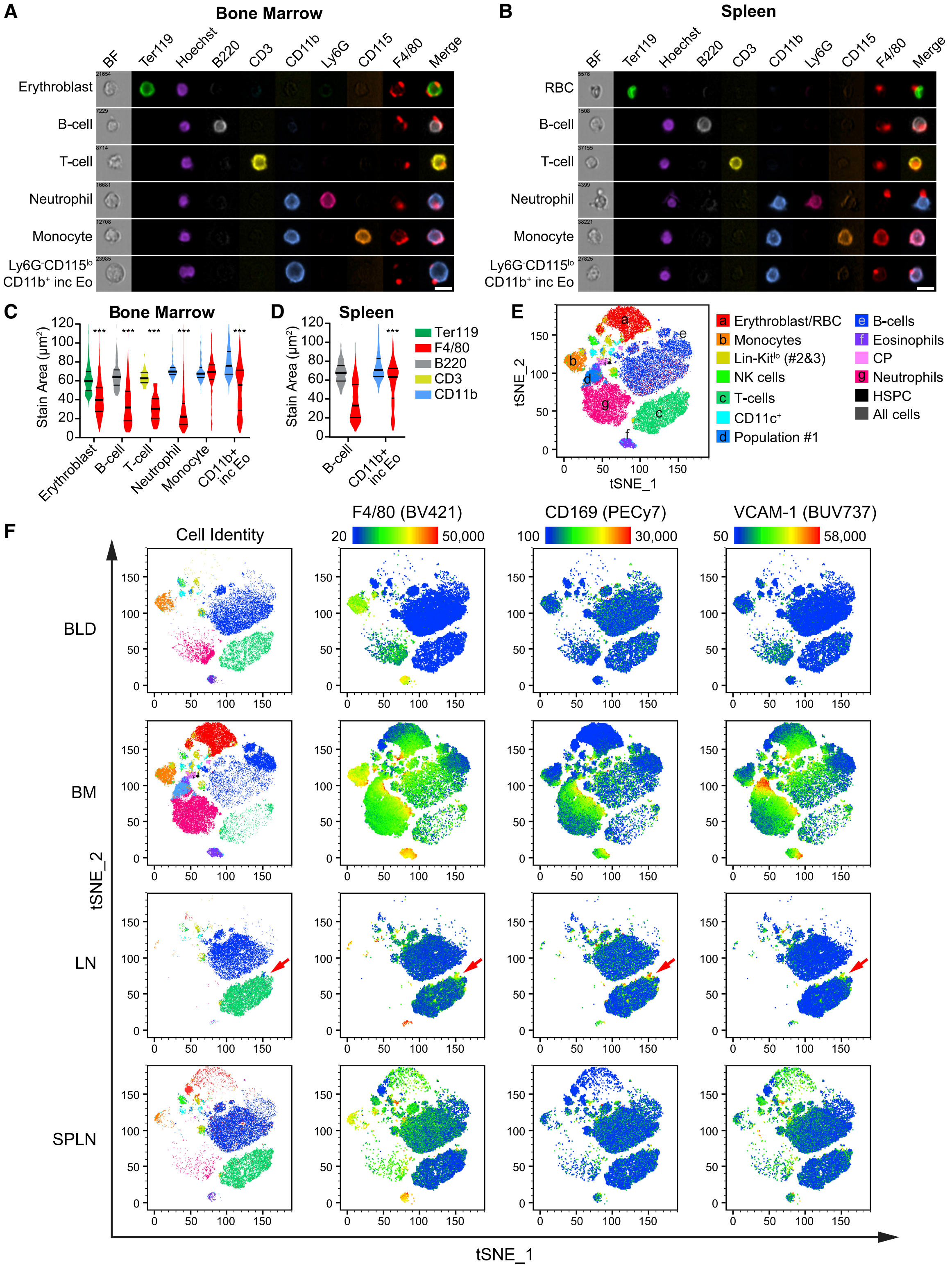

Figure 3. Macrophage markers are detected across many cell lineages in hematopoietic-tissue-derived cell suspensions

(A and B) Representative images of F4/80 staining associated with hematopoietic cell lineages that are not macrophages, as visualized in BM (A) and SPLN (B) using imaging flow cytometry according to the gating strategy outlined in Figure S4. The merge image consists of F4/80 with a relevant cell-surface marker

(legend continued on next page)

markers (excluding EGFP, F4/80, CD169, and VCAM-1) (Figure 3E). Each tissue was then assessed independently (Figure 3F), with the first column showing the cellular composition of the tissue and subsequent columns a heat-map representation of the staining intensity for macrophage markers F4/80, CD169, and VCAM-1. Peripheral blood was analyzed as a comparator sample that was obtained without mechanical disruption and that contained a similar profile of mature hematopoietic cells. In addition to the global overview of macrophage marker distribution provided by the t-SNE heatmaps, the frequency of macrophage marker staining on each defined cell type (gated as outlined in Figure 1) is shown in Figure S5. In blood, F4/80 staining was restricted to cells with confirmed endogenous-cell-surface F4/80 expression, and, as expected, CD169 and VCAM-1 were absent (Figure 3F; Figure S5D and S5E). In BM, subsets of all defined cell types had detectable F4/80, CD169 and VCAM-1 (Figure 3F), consistent with imaging flow cytometry showing macrophage remnants (Figure 3A).

The degree of macrophage marker promiscuity varied between tissues and between cell populations within tissues. For example, approximately 60% of BM, 15% of spleen, and 20% of lymph node T cells had detectable F4/80 expression (Figures 3E and 3F; Figures S5A–S5C), while peripheral blood T cells did not (Figures 3E and 3F; Figure S5D). Within lymph node, a portion of F4/80$^+$ T cells also had high intensity staining for CD169 and VCAM-1 (Figure 3F, arrows). In spleen, in addition to high-intensity F4/80 staining on cells with endogenous F4/80 expression (monocytes and eosinophils), many B cells had moderate intensity F4/80 staining, whereas CD169 and VCAM-1 staining were more restricted (Figure 3F; Figure S5B). This more selective pattern of remnant attachment raised the possibility that macrophage-remnant binding is not random. In spleen, F4/80$^+$CD169$^-$ macrophages are restricted to the red pulp, whereas CD169$^+$F4/80$^-$ metallophilic marginal zone macrophages are situated at the border of B cell follicles and the marginal zone (Idoyaga et al., 2009) (Figure 4A). Within the red pulp, there is a higher density of B cells than T cells (Figure 4A), and accordingly, *in situ* quantification showed a higher proportion of B220$^+$ (B cell marker) stain within close proximity of F4/80$^+$ stain compared to CD3 (T cell marker) stain (Figures 4A and 4B). Similarly, very few T cells were observed in the marginal zone with a higher proportion of B220$^+$ stain within close proximity of CD169$^+$ stain (Figures 4A and 4C). The distribution frequency of F4/80 and CD169 staining on B cells and T cells by flow cytometry (Figures 4D and 4E) followed a similar pattern, with more F4/80$^+$ events (Figure 4F) and more CD169$^+$F4/80$^-$ events (Figure 4G) observed within the B cell than the T cell gate. Hence, the macrophage-remnant profile on splenic lymphocytes correlated with their proximity to macrophages *in vivo*. This suggests that macrophage remnants preferentially adhere to cells with which they were interacting prior to mechanical disruption.

BM F4/80$^+$Ly6G$^+$ events exemplify the macrophage origin of F4/80$^+$ remnants

F4/80$^+$Ly6G$^+$ events in BM detected by traditional flow cytometry have previously been identified and purified as erythroblastic island macrophages (EIMs), also expressing VCAM-1, CD169, and ER-HR3 (Jacobsen et al., 2014; Li et al., 2019). Herein, imaging flow cytometry indicated that this dual expression is a consequence of macrophage-remnant binding to Ly6G$^+$ neutrophils (Figures 3A and 3B) and therefore is not an EIM-distinguishing phenotype. To confirm that the F4/80 remnant is donated from macrophages, we examined the impact of inducible depletion of all BM macrophage subsets using diphtheria toxin (DT) treatment of *Siglec1*$^{DTR/+}$ mice (Kaur et al., 2018; Miyake et al., 2007). DT treatment eliminated ramified F4/80^{hi} macrophages (Figure 5A). BM neutrophil frequency was maintained during DT treatment, whereas F4/80 co-staining on Ly6G$^+$ neutrophils was eliminated (Figures 5B and 5C). CD115^{hi} cells (myeloid progenitors and monocytes, which are CD169$^-$) were expanded, not depleted, in this model (Figures 5A, 5B, and 5D). Endogenous-cell-surface F4/80 staining on CD115^{hi} cells was maintained during DT treatment (Figures 5B and 5D). These results indicate that F4/80$^+$Ly6G$^+$ events represent fragmented F4/80$^+$Ly6G$^-$ macrophage remnants adhered to F4/80$^-$Ly6G$^+$ neutrophils.

CD169 is an adhesion molecule that binds to sialic acids and has been reported to mediate interactions between macrophages and other immune cells (Macauley et al., 2014). We investigated whether CD169 was essential for F4/80$^+$ remnant adhesion in *Siglec1*$^{DTR/DTR}$ (CD169-knockout [KO]) mice. These mice lack detectable CD169 protein in the BM (Figure 5E), but there is no impact on total F4/80$^+$ cells or their distribution (Figures 5E and 5F). Consistent with the first described CD169-KO model (Oetke et al., 2006), the immune cell composition of the BM was unchanged compared to wild-type mice (Table S3). In wild-type mice, the proportion of CD169$^+$ and F4/80$^+$ events was similar within hematopoietic stem and progenitor cell (HSPC) or granulocyte (neutrophil and eosinophil) populations, suggesting remnants attached to these cells had been donated by F4/80$^+$CD169$^+$ macrophages (Figure S5A). In CD169-KO mice, targeted inspection of HPSC, neutrophil, and eosinophil populations showed a selective robust reduction of F4/80$^+$ and VCAM-1$^+$ remnants, respectively (Figure 5G). These data indicate that CD169 contributes to the capacity of macrophages to interact with progenitors and other myeloid cells.

(Ter119, erythroblasts; B220, B cells; CD3ε, T cells; CD11b, neutrophils, monocytes, Ly6G$^-$CD115$^{lo/-}$CD11b$^+$ cells; this final population includes eosinophils). Scale bar, 10 μm.

(C and D) Paired comparison of stain area for a defining cell-surface marker compared to F4/80 for the cell populations displayed in (A) and (B). Data displayed as violin plots with median and 25th/75th percentiles. Kruskal-Wallis test with Dunn's correction for multiple comparisons; ***$p < 0.0001$. n = 26–1,086 for each cell type. Too few F4/80$^+$ splenic T cells, neutrophils, and monocytes were captured in the imaging flow cytometry assay for statistical analysis.

(E) Mapping of hematopoietic cell lineages in conventional flow cytometry data pooled from peripheral blood, BM, LN, and SPLN to a t-SNE plot. Indicated cell types are gated as outlined in Figures 1A and S1.

(F) For each tissue, the t-SNE plot is used to display cell composition (first column, color-coded according to E) and a heatmap of staining intensity for the macrophage-expressed surface markers F4/80, CD169, and VCAM-1 (subsequent columns). A hot spot of macrophage marker staining on LN T cells is indicated (red arrows).

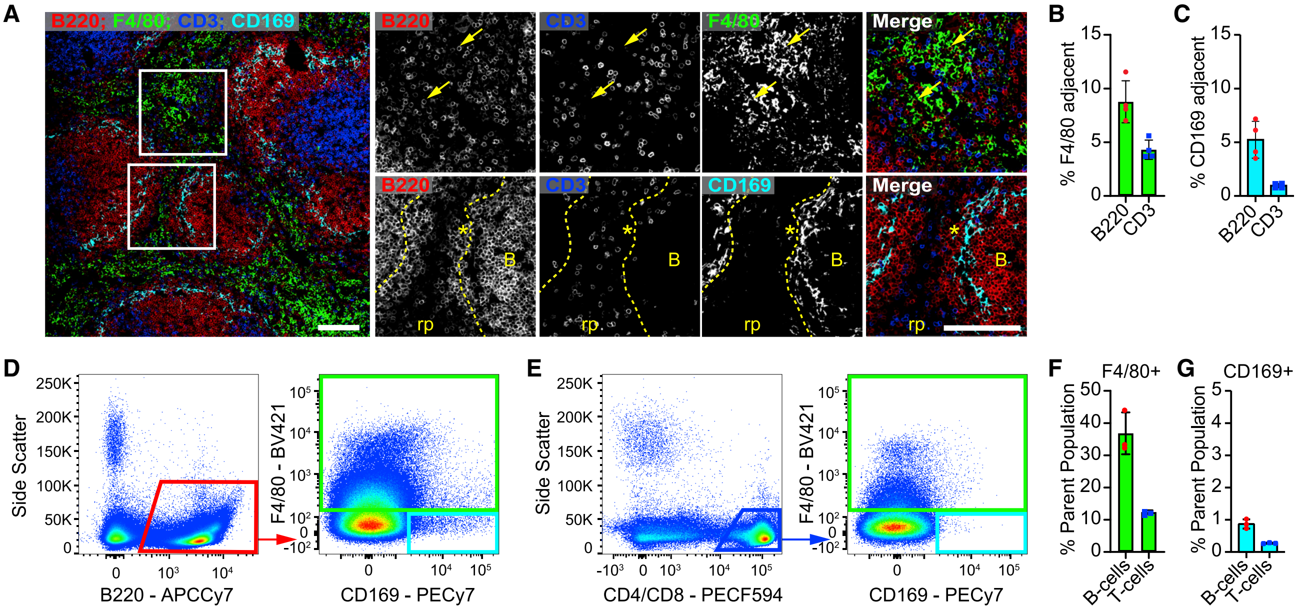

Figure 4. Extent of lymphocyte colocalization with splenic macrophage subsets *in situ* is consistent with promiscuous macrophage marker staining on dissociated splenic lymphocytes

(A) Cryosections of C57BL/6J mouse SPLN stained for B cells (B220), T cells (CD3), red pulp (rp) macrophages (F4/80), and metallophilic marginal zone macrophages (CD169). The top panel images highlight a region of red pulp where B cells are more populous than T cells and more likely to be present in areas with intense F4/80 staining (yellow arrows). The bottom panel images highlight a region where CD169$^+$ macrophages demarcate the boundary between the B cell follicle (yellow "B") and marginal zone (yellow asterisk). In this image, T cells are mostly restricted to the small area of red pulp visible between the follicles. Scale bars, 100 μm.

(B) Assessment of the colocalization of B cells and T cells with red pulp macrophages by quantitation of the frequency of B220 or CD3 staining adjacent to F4/80 staining (within 3 pixels). Data are represented as mean ± SD; n = 4.

(C) Assessment of the colocalization of B cells and T cells with metallophilic marginal zone macrophages by quantitation of the frequency of B220 or CD3 staining adjacent to CD169 staining (within 3 pixels). Data are represented as mean ± SD; n = 4.

(D and E) Gating strategy used to assess the frequency of B cells (D) and T cells (E) that were either F4/80$^+$ or CD169$^+$F4/80$^-$. Data was pre-gated, as shown in Figure S1A.

(F and G) Frequency of B cells and T cells that are either F4/80$^+$ (F) or CD169$^+$F4/80$^-$ (G) by flow cytometric analysis. Data are represented as mean ± SD; n = 3.

Macrophage remnants include cytoplasmic components

In BM isolated from *Siglec1*^{Cre};*R26*^{ZsGreen} animals, 87% ± 2% of CD45$^+$F4/80$^+$ events were classified by visual inspection as CD45$^+$ cells with associated F4/80$^+$ subcellular remnants (Figure 6A). Significantly, 52% ± 7% of these cells had detectable cytoplasmic ZsGreen reporter colocalized with at least one attached remnant (Figures 6A and 6B). While rare events with demonstrable intracellular ZsGreen were observed, these appeared to be ZsGreen$^+$ cells with associated F4/80$^+$ remnants rather than a population of intact F4/80$^+$ZsGreen$^+$ cells (Figure 6A). Figure 6C shows confocal imaging of an F4/80$^+$ remnant attached to a B220$^+$ B cell within freshly isolated BM single-cell suspension, reproducing the remnant observation using an independent technique similar to one previously used (Lynch et al., 2018). F4/80 and B220 staining are clearly present on the membrane of the subcellular remnant and intact cell, respectively, and ZsGreen fluorescence was encapsulated within F4/80$^+$ membrane (Figure 6C). The imaged subcellular remnant is 1 to 2 μm in diameter, making it substantially larger than the typical 50- to 500-nm extracellular microvesicle (van Niel et al., 2018) or 30- to 100-nm exosome (Doyle and Wang, 2019).

To determine whether macrophage mRNA is retained within remnants and contributes to bulk cell-sorted expression profiles, we isolated HSPCs and committed progenitors (CPs). These cell populations were chosen because they do not natively express mature macrophage genes, and macrophages influence their niche *in vivo* via direct cell interactions (Hur et al., 2016). Both imaging (Figure 6D) and conventional (Figures 6E and 6F) flow cytometry analysis of CD117/Kit$^+$-enriched BM confirmed attachment of F4/80$^+$ macrophage remnants containing ZsGreen cytoplasmic reporter on all HSPC subsets (gated as outlined in Figures S6A and S6B). Sorted CPs (sub-fractioned based on F4/80 and ZsGreen detection) and total HSPCs all demonstrated equivalent expression levels of the stem cell marker, *Kit* (Figures 6G and 6H). Macrophage-marker transcripts were readily detectable in total HSPC and were present in F4/80$^+$ CP populations at comparable levels to *in vitro*-differentiated BM-derived macrophages (Figures 6G and 6I). The exclusion of F4/80$^+$ events from the CP population eliminated detection of not only *Adgre1* (encoding the F4/80 antigen-containing protein) but also mRNA for macrophage markers *Aif1, Cd68*, and *Mertk* (Figures 6G and 6I). Conversely, exclusion of ZsGreen$^+$ events from sorted

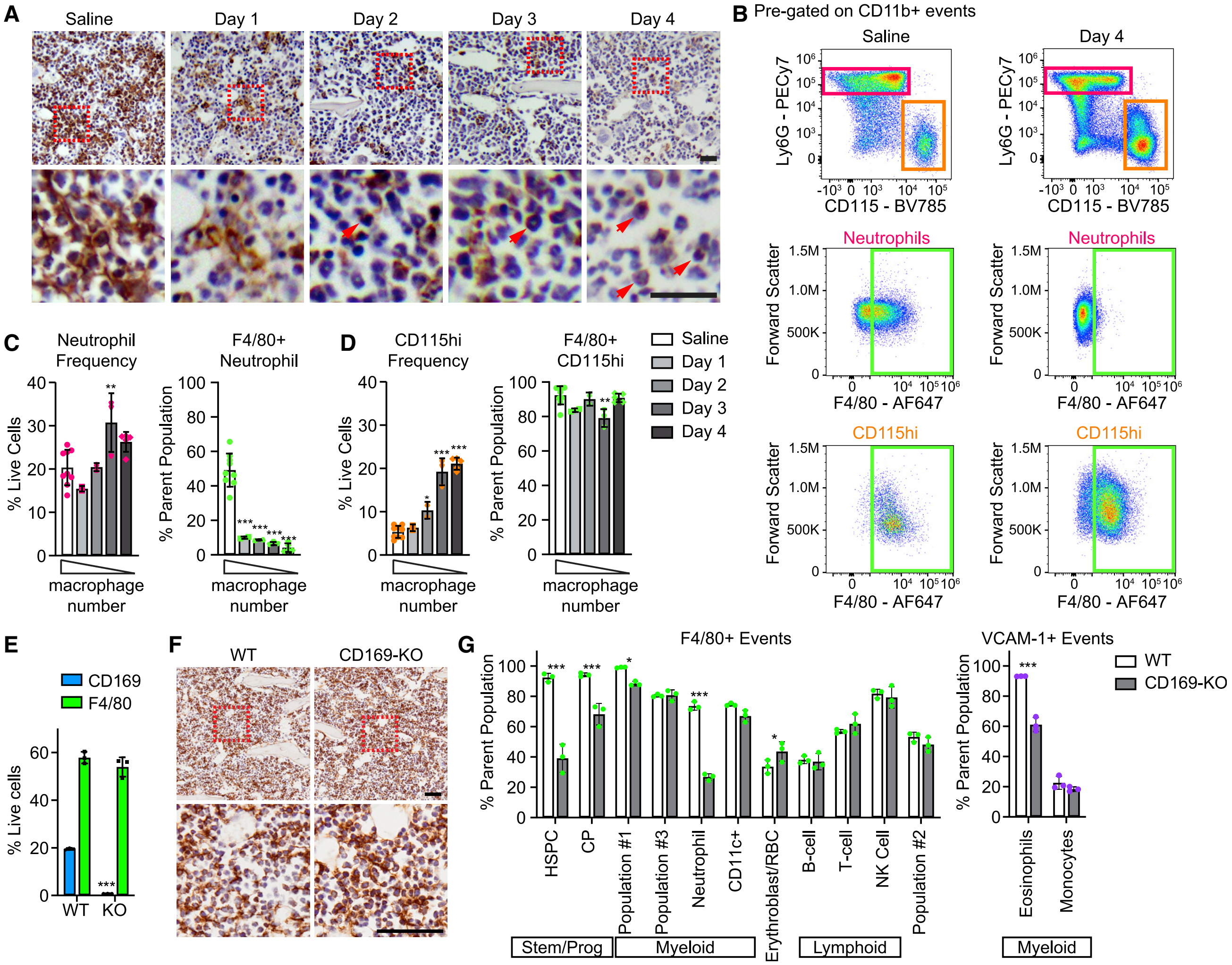

Figure 5. CD169$^+$ macrophage depletion eliminates F4/80$^+$ remnant staining, and CD169-knock out (KO) selectively modulates the F4/80$^+$ remnant profile

(A) CD169$^+$ macrophages were depleted in *Siglec1*$^{DTR/+}$ mice by daily 10 μg/kg diphtheria toxin (DT) injections, starting on day 0. Reduced numbers of ramified F4/80$^+$ macrophages are evident at day 1, with complete elimination of these cells by day 4. Red arrowheads indicate cells with endogenous F4/80 expression that lack macrophage morphology. Scale bars, 25 μm.

(B) Representative flow cytometry plots of BM from saline-treated control mice (top panel) and at day 4 of DT-mediated macrophage depletion (bottom panel). Neutrophils (magenta gate) and CD115^{hi} (orange gate) populations were gated from CD11b$^+$ BM, and F4/80$^+$ events (green gate) assessed.

Data are represented as mean ± SD; n = 2-9 depending on the time point. (C) No adverse impacts on neutrophil frequency were observed across the macrophage depletion time course, whereas F4/80 staining on neutrophils was eliminated. One-way ANOVA with subsequent comparison to saline control using Dunnett correction for multiple comparisons; **p = 0.004, ***p < 0.0001.

(D) The frequency of BM CD115^{hi} cells, including monocytes and myeloid precursors, increases over the macrophage depletion time course, and they maintain F4/80$^+$ staining. Data are represented as mean ± SD; n = 2–9 depending on the time point. One-way ANOVA with subsequent comparison to saline control using Dunnett correction for multiple comparisons; *p = 0.02, **p = 0.006, ***p < 0.0001.

(E) KO of the macrophage-specific adhesion molecule, CD169, in *Siglec1*$^{DTR/DTR}$ mice is confirmed by conventional flow cytometry for CD169$^+$ events in total BM. The frequency of F4/80$^+$ events in total BM is not impacted by CD169-KO.

(F) F4/80$^+$ cell morphology and distribution in bone marrow is unaltered by CD169-KO. Scale bars, 25 μm.

(G) CD169-KO selectively reduces the frequency of F4/80$^+$ or VCAM-1$^+$ macrophage remnants on granulocytes and hematopoietic stem/progenitor cells (HSPCs) in BM. Populations were gated as outlined in Figure 1A. Two-way ANOVA with subsequent comparison between wild-type (WT) and CD169-KO using Sidak correction for multiple comparisons. *p = 0.05, ***p < 0.0001.

F4/80$^+$ CPs did not impact the detection of macrophage-specific genes (Figures 6G and 6I), indicating that mRNA detection sensitivity exceeded fluorescent reporter detection in this assay.

We examined RNA-seq data from BM cells sorted from *Csf1r*-EGFP mice by positive selection for macrophage markers (gated as outlined in Figure S7A). The most abundant transcripts in these positively selected populations were not enriched within

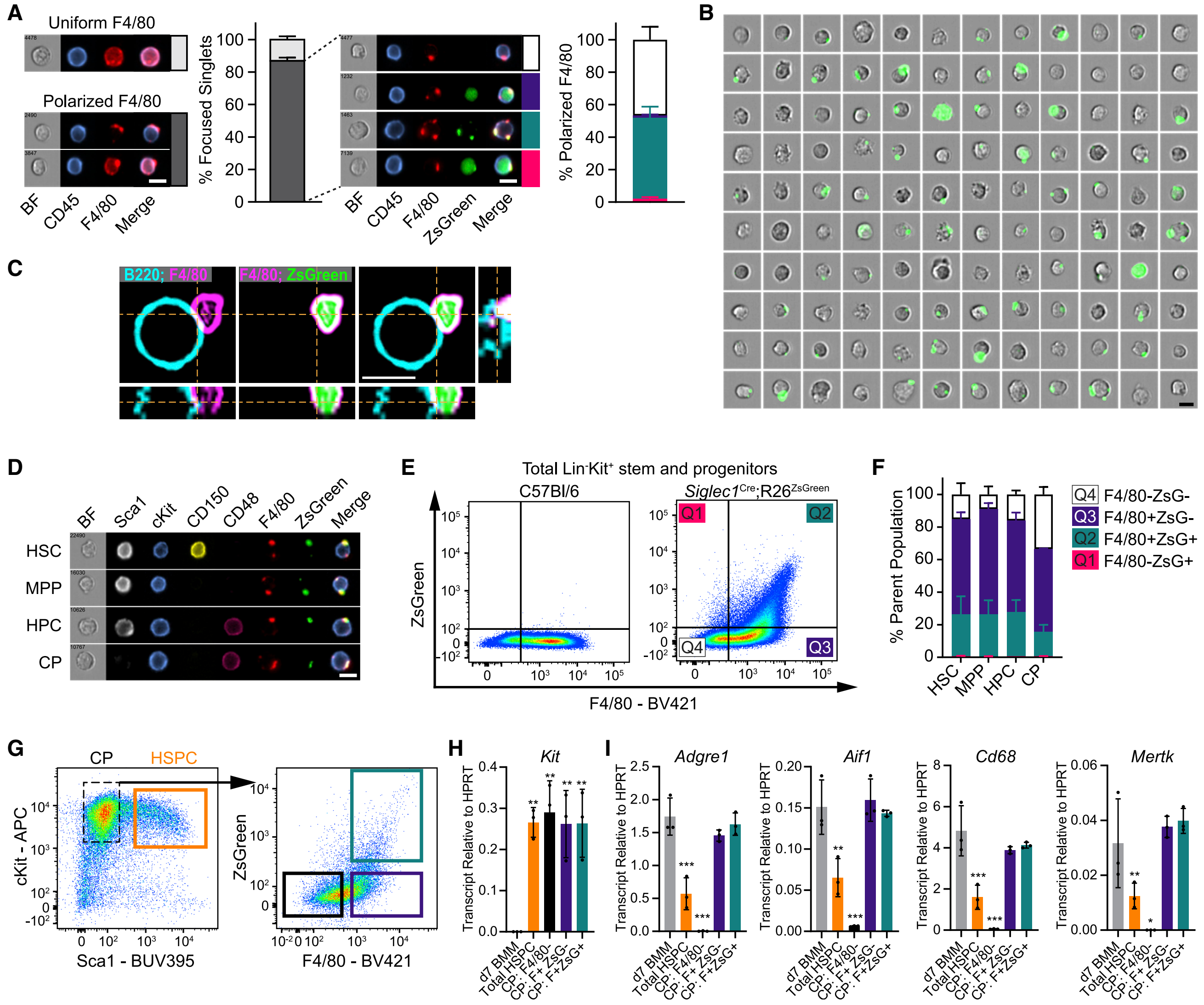

Figure 6. Macrophage remnants contain cytoplasm and contribute to the RNA profile of sorted non-macrophage cell populations

(A) BM isolated from *Siglec1*^{Cre};*R26*^{ZsGreen} mice was visualized by imaging flow cytometry. CD45$^+$F4/80$^+$ events were manually categorized by whether F4/80 staining was polarized or uniformly and exclusively cell surface. Polarized events were further categorized based on whether ZsGreen was observed in the primary cell event and/or associated with F4/80 remnant staining. Scale bar, 10 μm. Graphical data are represented as mean ± SD; n = 4.

(B) Image gallery displaying ZsGreen fluorescence overlay on BF images for a representative selection of CD45$^+$F4/80$^+$ events analyzed in (A). Scale bar, 10 μm.

(C) Confocal imaging of a *Siglec1*^{Cre};*R26*^{ZsGreen} B cell in BM cell suspension stained for F4/80 (magenta) and B220 (cyan), shown in orthangonal view. Scale bar, 5 μm.

(D) F4/80$^+$ZsGreen$^+$ macrophage remnants visualized on all HSPC subsets in Kit-enriched BM from *Siglec1*^{Cre};*R26*^{ZsGreen} mice. HSPC subsets (CD48$^+$ hematopoietic progenitor cell [HPC], CD48$^-$CD150$^-$ multipotent progenitor (MPP), and CD48$^-$CD150$^+$ hematopoietic stem cell [HSC]) were gated, as outlined in Figure S6A. Scale bar, 10 μm.

(E and F) Frequency of F4/80$^+$ZsGreen$^+$ staining on HSPC subsets enumerated by conventional flow cytometry. The quadrant gates shown for total Lin$^-$Kit$^+$ cells (E) were applied to each HSPC subset, gated as outlined in Figure S6B, and graphed in (F). Data are represented as mean ± SD; n = 3.

(G–I) Kit-enriched BM pooled from *Siglec1*^{Cre};*R26*^{ZsGreen} mice was sorted into four populations (G) for subsequent RNA expression analysis. Expression of the HSPC marker, *Kit* (H), and macrophage expressed markers (I; *Adgre1*, *Aif1*, *Cd68*, *Mertk*) in the HSPC and CP subsets shown in (G) as compared to *in vitro*-differentiated BM macrophages (d7 BMM). Data are represented as mean ± SD; n = 3 independent sorts. One-way ANOVA with Dunnett correction for multiple comparisons; *p = 0.046, **p < 0.005, ***p < 0.0001.

the ImmGen ULI-RNA-seq monocyte/macrophage datasets (GEO: GSE127267). Rather, the CD11b$^+$ "macrophage" population (CD11b$^+$F4/80$^+$Ly6G$^-$EGFP^{lo}VCAM-1$^+$) displayed a granulocyte signature (Figure 7A). Applying predictions based on the remnant-binding profile exemplified in Figure S5A, this sort strategy would be anticipated to isolate a mixed granulocyte population comprised of CD11b$^+$F4/80$^+$ eosinophils and CD11b$^+$Ly6G$^-$EGFP^{lo} neutrophil precursors (population 1;

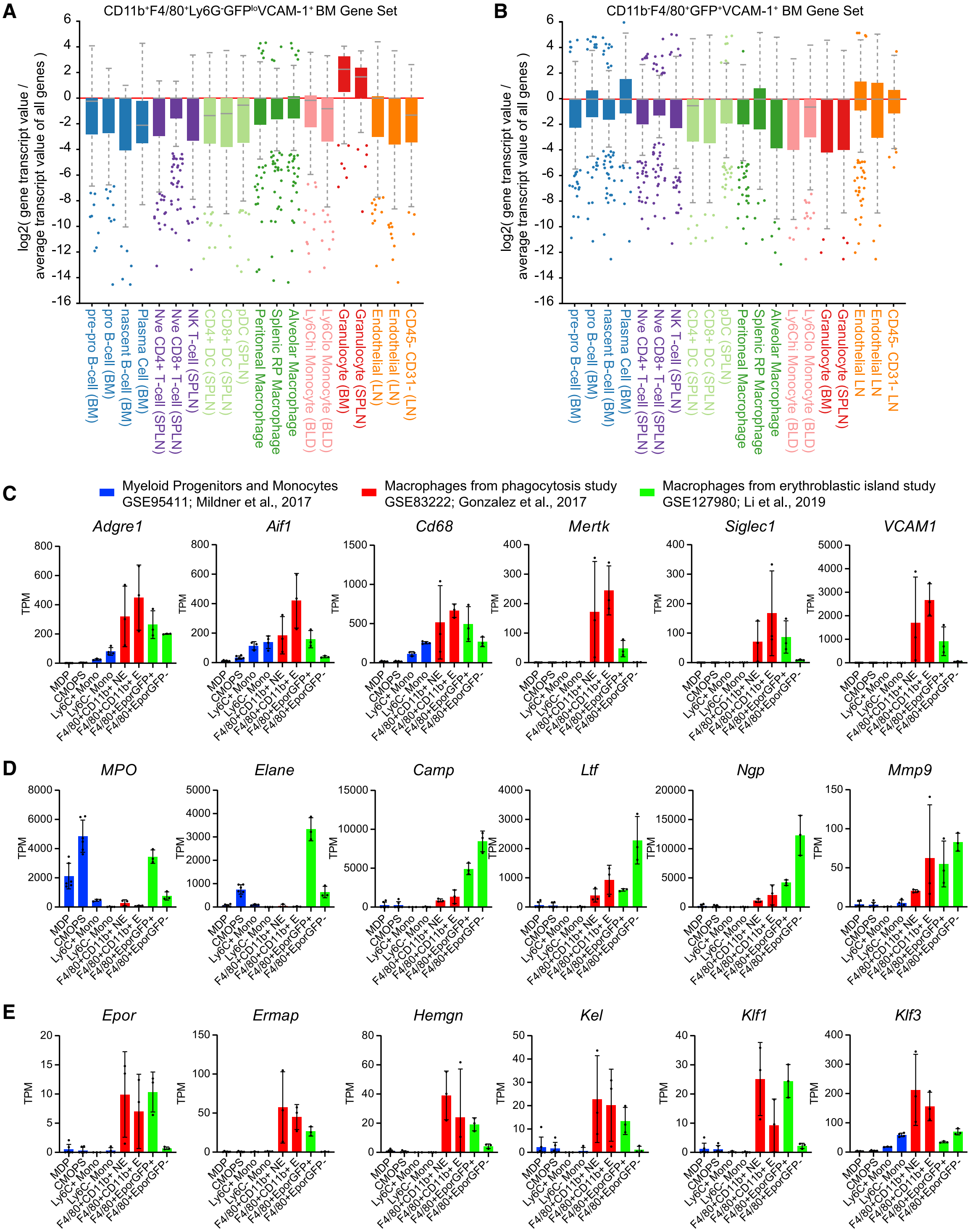

Figure 7. RNA-seq data from sorted BM macrophage populations is consistent with non-macrophage cells contaminated with RNA-laden macrophage remnants

(A and B) CD11b$^+$ (A) and CD11b$^-$ (B) BM populations were sorted based on positive macrophage marker selection, as outlined in Figure S7A, and subjected to RNA-seq analysis. The prevalence of the top 200 most abundant transcripts from each population is displayed across a subset of the ImmGen ULI RNA-seq dataset (GEO: GSE127267). Similar analysis for a CD11b$^+$ BM population sorted by an alternate strategy is shown in Figure S7B.

(C–E) Transcript abundance data for monocyte-macrophage marker transcripts (C), neutrophil marker transcripts (D), and erythroblastic marker transcripts (E) are displayed for publicly available BM monocyte-macrophage samples from three studies, as indicated in the legend. GEO: GSE95411 (blue) was comprised of

(legend continued on next page)

Figure 1A) with bound F4/80^{+} remnants, thus explaining the observed gene signature. An alternate sorting strategy for CD11b^{+} "macrophages" (CD11b^{+}F4/80^{+}CD169^{+}CX3CR1^{-}) without Ly6G-negative selection also exhibited a clear granulocyte signature (Figure S7B). The CD11b^{-} "macrophage" population (CD11b^{-}F4/80^{+}EGFP^{+}VCAM1^{+}) showed a weak similarity with plasma cells and lymph node endothelial cells (Figure 7B). Endogenous EGFP expression within plasma cells, resulting from Csf1r promoter activity driven by the transcription factor PU.1 in these cells (Ross et al., 1994, 1998), likely contributed to their enrichment within this population. Erythroblasts are a major CD11b^{-} BM cell lineage not represented in the ImmGen ULI-RNA-seq data. Erythroblast-expressed genes, including *Kel*, *Ermap*, *Ank1*, *Ache*, *Ackr1*, and *Redrum*, were also present within the most abundant transcripts from the CD11b^{-} "macrophage" population (data not shown). These data confirm that BM populations positively selected for macrophage marker expression are comprised of macrophage remnants adhered to mixed populations of non-macrophage cells.

Publicly available and previously curated (Summers et al., 2020) RNA-seq datasets of BM monocytes and macrophages (A-Gonzalez et al., 2017; Li et al., 2019; Mildner et al., 2017) were analyzed independently to determine whether they were similarly confounded by macrophage remnants. Analysis of monocytes and precursors isolated from BM (blue columns in Figures 7C–7E) showed that progenitor cells did not express macrophage markers but had strong expression of neutrophil markers, while monocyte populations isolated from BM expressed myeloid genes but not transcripts for macrophage-specific markers (Figure 7C), neutrophil markers (Figure 7D), or erythroblast markers (Figure 7E). In a study of macrophage phagocytosis (red columns in Figures 7C–7E), the presence of macrophage-specific RNA in sorted macrophages was confirmed by detection of *Mertk*, *Siglec1*, and *Vcam1* transcripts (Figure 7C). Similarly, macrophages isolated from erythroblastic islands (green columns in Figures 7C–7E) showed expression of macrophage markers (Figure 7C). However, these positively selected macrophage populations frequently had granulocyte markers at a higher abundance than macrophage markers (Figure 7D) and also had detectable erythroblast transcripts (Figure 7E). The transcript profile of sorted monocyte populations is consistent with a distinct cell population of the expected identity, whereas the transcript profile of macrophage populations is consistent with contributions from multiple cell types.

Independent validation of these observations was also achieved by analysis of macrophage populations within the Tabula Muris, a high-profile compendium of single-cell transcriptome data from the mouse generated by fluorescence-activated cell sorting (FACS) or droplet isolation (Tabula Muris Consortium et al., 2018). In the BM and spleen single-cell FACS datasets, only 3.4% of total BM and 2.8% of spleen cells were identified as macrophages. Very few of these cells had detectable expression of the macrophage marker genes *Csf1r, Adgre1*, and *Siglec1*. Indeed, only a low proportion of these cells expressed a panel of myeloid lineage markers (Table S4), suggesting that the single-cell analysis approach did not capture macrophages in these tissues. In contrast, other myeloid cells were preserved and expressed appropriate gene profiles (Table S4). Table S5 shows that within the Tabula Muris BM dataset, *Csf1r* was detected in a portion of a large range of cell types that do not express *Csf1r* mRNA or protein *in vivo* (Grabert et al., 2020), including immature and mature lymphocytes (18% of BM mature B cells had detectable *Csf1r* mRNA). A range of other myeloid/macrophage-specific genes were also detected (Table S5). This analysis provides independent confirmation that myeloid mRNAs contaminate non-myeloid cell populations in scRNA-seq datasets of hematopoietic tissues.

DISCUSSION

Our data provide comprehensive evidence that intact macrophages are not present within *ex vivo* cell preparations from hematopoietic tissues, as they are mechanically disrupted during preparation of cell suspensions. A negative gating strategy showed that non-macrophage cell types account for over 98% of cells within these tissue cell suspensions. Positive staining for macrophage markers was a consequence of other cells being cloaked with remnants. These observations are consistent with the report that subcapsular sinus macrophages are fragmented during lymph node single-cell preparation and attached to interleukin (IL)-7-receptor-expressing T cells (Gray et al., 2012). Key observations made herein were that the cell-attached macrophage remnants contained not only membrane and associated proteins at high molecular density but also intracellular contents, including significant amounts of mRNA. This technical phenomenon has contributed to the misassignment of macrophage identity to flow-cytometry-gated populations in hematopoietic tissues, including our own studies reporting F4/80^{+}Ly6G^{+} cell events as EIMs (Jacobsen et al., 2014; Kaur et al., 2018). Indeed, Li et al. (2019) used a distinct approach to isolate and profile F4/80^{+} EIMs based upon an *Epor*-EGFP transgene, but our analysis herein of their data revealed strong enrichment for immature myeloid transcripts in the putative EIMs. Nonetheless, we showed that these *ex vivo* analyses can still provide valuable and robust biological information. Coupling conventional flow cytometry with *in situ* approaches (Kaur et al., 2018) or bespoke isolation strategies that maintain multicellular aggregates (Bisht et al., 2020; Seu et al., 2017; Tay et al., 2020; Yeo et al., 2016, 2019) strengthens data interpretation and confirms some

---

myeloid progenitor and monocyte populations. GEO: GSE83222 (red) and GEO: GSE127980 (green) were comprised of positively selected macrophage populations. TPM, transcripts per million. All data are represented as mean ± SD; n = 3. These data were extracted from a comprehensive meta-analysis of RNA-seq data from the mouse mononuclear phagocyte system. The sorted populations displayed are: macrophage-dendritic cell progenitors (MDPs; Lin^{-}CD115^{hi-}Kit^{+}CD135^{+}Ly6C^{-}CD11b^{lo}), monocyte-committed common monocyte progenitors (cMoPs; Lin^{-}CD115^{hi}Kit^{+}CD135^{-}Ly6C^{hi}CD11b^{lo}), Ly6C^{+} and Ly6C^{-} monocytes (Monos; Lin^{-}CD115^{hi}Kit^{-}CD135^{-}CD11b^{+}) (blue columns), F4/80^{+}CD11b^{+} cells designated as non-engulfing (NE; non-phagocytic) or engulfing (E; phagocytic) macrophages based on detection of DsRed from a parabiotic partner (red columns), and F4/80^{+} events segregated by *Epor*-EGFP expression (green columns).

instances of unconventional co-expression of immune markers (Abtin et al., 2014; Yates et al., 2013).

Macrophage remnants are similar in size to oncosomes, the largest described plasma-membrane derived microvesicles (van Niel et al., 2018). As intact macrophages could not be identified within hematopoietic tissue preparations, it is unlikely that remnants represent extracellular vesicles shed by macrophages *in vivo*. Rather, it appears that the integrity of highly ramified tissue-resident macrophages has been disrupted *en masse* by the fluid and/or mechanical shear stress inherent in preparing hematopoietic tissue single-cell suspensions. Given the absence of an intended vesicular budding/fission event, it is remarkable that macrophage disruption results in structurally stable remnants that retain intracellular contents. Our presumption is that macrophages fail at their structurally narrowest points, facilitating membrane fusion due to the self-healing capacity of lipid membranes (Sych et al., 2018).

Our results cannot distinguish whether the presence of remnants reveals *in vivo* cell-cell interactions or reflects attachment of remnants to cell populations with appropriate molecular-adhesion profiles during isolation. We favor the former interpretation. While the preferential binding of F4/80$^+$CD169$^-$ macrophage remnants to erythroblasts is difficult to reconcile with previous evidence (Bisht et al., 2020; Chow et al., 2013; Seu et al., 2017; Tay et al., 2020), it is consistent with *in vitro* experiments demonstrating that murine CD169 binds neutrophils, not murine erythrocytes (Kelm et al., 1994). Furthermore, our data suggests that neutrophil-associated macrophage remnants are F4/80$^+$CD169$^+$, with CD169-KO reducing remnant binding to neutrophils but not erythroblasts.

The disruption of macrophages during tissue disaggregation is not surprising, given their remarkable ramification and adhesive properties (Grabert et al., 2020). Kupffer cell disruption and remnant binding to liver endothelial cells has been previously visualized (Lynch et al., 2018). Contrasting with our observations in hematopoietic tissues, intact Kupffer cells were also detectable in these liver cell preparations (Lynch et al., 2018). Meta-analysis of bulk sequencing data of sorted cell populations across 14 different tissues demonstrated that contamination of macrophage datasets with genes expressed by unrelated cell types is universal (Summers et al., 2020). The reciprocal contamination is also a significant issue, likely leading to the false assignment of expression of macrophage-enriched genes such as *Csf1r* to non-macrophages. Tissue digestion of spleen did not markedly change the splenic myeloid flow cytometry profile compared to mechanical disruption (Fujiyama et al., 2019). Enzymatic tissue digestion does not prevent macrophage fragmentation, although it may facilitate isolation of subsets of intact macrophages from some tissues, including liver (Lynch et al., 2018) and lung (Becher et al., 2014; Misharin et al., 2013).

Macrophage fragmentation and remnant binding likely explain why macrophage signatures are poorly represented or challenging to interpret in large-scale molecular studies of organ biology (Baccin et al., 2020; Becher et al., 2014; Gautier et al., 2012; Tabula Muris Consortium et al., 2018). On the basis of the Tabula Muris data (Tabula Muris Consortium et al., 2018), one would conclude that *Csf1r* is widely present in non-hematopoietic cells, which is clearly not the case (Grabert et al., 2020). Indeed, herein and previously (Kaur et al., 2021), we corrected the record relating to HSPC expression of CSF1R (Mossadegh-Keller et al., 2013). Our results may also reflect why mapping of BM macrophage origin has been conspicuously absent from comprehensive ontogeny studies (Ginhoux and Guilliams, 2016; Liu et al., 2019) and suggest that systematic assessments (Abram et al., 2014; Baccin et al., 2020) of single-cell preparations are insufficient for evaluating tissue-resident macrophages. Overall, our observations expose that the current knowledge base is incomplete and probably incorrect with respect to tissue-resident macrophage frequency, diversity, and molecular profile.

Limitations of the study

Hematopoietic tissue single-cell preparations were the focus, as they have high macrophage density and subpopulation complexity. Gaps in knowledge relating to these prominent cell populations were becoming more evident in emerging whole-organ transcriptomic datasets (Baccin et al., 2020). In-depth analysis of macrophage fragmentation in other tissues is needed and has already been suggested (Lynch et al., 2018). Confirmation that the degree of macrophage fragmentation consistently occurs regardless of strain, species, and age is also needed, with analysis of human hematopoietic tissues a priority, given the morphological and composition variations in human compared to mouse BM. We have also not been able to provide a solution to avoid/limit macrophage fragmentation or remove the associated remnants.

We have provided only limited evidence that mistaken identification of hematopoietic tissue macrophages or misattribution of macrophage-expressed genes has substantially impacted the current knowledge base. Exposure of the phenomenon will accelerate deconvolution of the macrophage blind spot exposed herein. Similarly, low macrophage representation and the detection of non-macrophage cells expressing macrophage-restricted genes in high-coverage scRNA-seq datasets is already appreciable but rarely acknowledged. As the depth of particularly scRNA-seq technologies increases, the impact of macrophage fragmentation will become an increasing specificity and accuracy hurdle. CITE-seq will not eliminate this issue, as cells carrying macrophage remnants are indistinguishable from other singlets by flow cytometry and contain macrophage protein and RNA.

STAR★METHODS

Detailed methods are provided in the online version of this paper and include the following:

- KEY RESOURCES TABLE
- RESOURCE AVAILABILITY
    - ○ Lead contact
    - ○ Materials availability
    - ○ Data and code availability
- EXPERIMENTAL MODEL AND SUBJECT DETAILS
- METHOD DETAILS
    - ○ Macrophage depletion
    - ○ Thioglycollate-elicited macrophages

  - ○ Tissue harvesting and processing
  - ○ 2.4G2 hybridoma supernatant
  - ○ Flow cytometry
  - ○ Imaging flow cytometry
  - ○ Immunofluorescent staining and imaging
  - ○ Immunohistochemical staining
  - ○ Bulk RNA analysis of sorted cell populations
- ● QUANTIFICATION AND STATISTICAL ANALYSIS

SUPPLEMENTAL INFORMATION

Supplemental information can be found online at https://doi.org/10.1016/j.celrep.2021.110058.

ACKNOWLEDGMENTS

This work was supported by Mater Foundation, The UQ Postgraduate Scholarship, and Mater Research Frank Clair Scholarship (L.B.); a Veronika Sacco Clinical Cancer Research Fellowship from the Florey Medical Research Foundation; University of Adelaide (J.E.N.); a NHMRC Research Fellowship (1136130, J.-P.L.); and an ARC Future Fellowship (FT150100335, A.R.P.). Dr. Julie Davis contributed experimental resources. The majority of this work was carried out at the Translational Research Institute (TRI), which is supported by a grant from the Australian Government. The TRI Microscopy, Histology, Biological Research Facility, and Flow Cytometry Core Facilities contributed technical expertise. Graphical abstract was created with BioRender.com.

AUTHOR CONTRIBUTIONS

Conceptualization, S.M.M., A.S., J.-P.L., D.A.H., L.J.R., and A.R.P.; methodology, S.M.M., O.H., A.S., S.K., A.C.P., D.P.S., K.M.S., and L.J.R.; validation, K.S.O.; formal analysis, S.M.M., A.S., K.M.I., K.M.S., A.C.P., and A.R.P.; investigation, S.M.M., O.H., K.S.O., A.S., S.K., C.J.S., A.C.W., G.W.M., K.M.S., and L.B.; writing – original draft, S.M.M. and A.R.P.; writing – review & editing, S.M.M., K.M.S., A.C.P., J.-P.L., D.A.H., and A.R.P.; supervision, S.M.M., J.E.N., A.C.W.Z., and A.R.P.; funding acquisition, J.-P.L., D.A.H., L.J.R., and A.R.P.

DECLARATION OF INTERESTS

The authors declare no competing interests.

Received: April 21, 2021
Revised: September 28, 2021
Accepted: November 3, 2021
Published: November 23, 2021

REFERENCES

A-Gonzalez, N., Quintana, J.A., García-Silva, S., Mazariegos, M., González de la Aleja, A., Nicolás-Ávila, J.A., Walter, W., Adrover, J.M., Crainiciuc, G., Kuchroo, V.K., et al. (2017). Phagocytosis imprints heterogeneity in tissue-resident macrophages. J. Exp. Med. *214*, 1281–1296.

Abram, C.L., Roberge, G.L., Hu, Y., and Lowell, C.A. (2014). Comparative analysis of the efficiency and specificity of myeloid-Cre deleting strains using ROSA-EYFP reporter mice. J. Immunol. Methods *408*, 89–100.

Abtin, A., Jain, R., Mitchell, A.J., Roediger, B., Brzoska, A.J., Tikoo, S., Cheng, Q., Ng, L.G., Cavanagh, L.L., von Andrian, U.H., et al. (2014). Perivascular macrophages mediate neutrophil recruitment during bacterial skin infection. Nat. Immunol. *15*, 45–53.

Baccin, C., Al-Sabah, J., Velten, L., Helbling, P.M., Grünschläger, F., Hernández-Malmierca, P., Nombela-Arrieta, C., Steinmetz, L.M., Trumpp, A., and Haas, S. (2020). Combined single-cell and spatial transcriptomics reveal the molecular, cellular and spatial bone marrow niche organization. Nat. Cell Biol. *22*, 38–48.

Barbier, V., Winkler, I.G., Wadley, R., and Lévesque, J.P. (2012). Flow cytometry measurement of bone marrow perfusion in the mouse and sorting of progenitors and stems cells according to position relative to blood flow in vivo. Methods Mol. Biol. *844*, 45–63.

Batoon, L., Millard, S.M., Wullschleger, M.E., Preda, C., Wu, A.C., Kaur, S., Tseng, H.W., Hume, D.A., Levesque, J.P., Raggatt, L.J., and Pettit, A.R. (2019). CD169$^+$ macrophages are critical for osteoblast maintenance and promote intramembranous and endochondral ossification during bone repair. Biomaterials *196*, 51–66.

Becher, B., Schlitzer, A., Chen, J., Mair, F., Sumatoh, H.R., Teng, K.W., Low, D., Ruedl, C., Riccardi-Castagnoli, P., Poidinger, M., et al. (2014). High-dimensional analysis of the murine myeloid cell system. Nat. Immunol. *15*, 1181–1189.

Bisht, K., Brunck, M.E., Matsumoto, T., McGirr, C., Nowlan, B., Fleming, W., Keech, T., Magor, G., Perkins, A.C., Davies, J., et al. (2019). HIF prolyl hydroxylase inhibitor FG-4497 enhances mouse hematopoietic stem cell mobilization via VEGFR2/KDR. Blood Adv. *3*, 406–418.

Bisht, K., Tay, J., Wellburn, R.N., McGirr, C., Fleming, W., Nowlan, B., Barbier, V., Winkler, I.G., and Levesque, J.P. (2020). Bacterial Lipopolysaccharides Suppress Erythroblastic Islands and Erythropoiesis in the Bone Marrow in an Extrinsic and G- CSF-, IL-1-, and TNF-Independent Manner. Front. Immunol. *11*, 583550.

Blériot, C., Chakarov, S., and Ginhoux, F. (2020). Determinants of Resident Tissue Macrophage Identity and Function. Immunity *52*, 957–970.

Chang, M.K., Raggatt, L.J., Alexander, K.A., Kuliwaba, J.S., Fazzalari, N.L., Schroder, K., Maylin, E.R., Ripoll, V.M., Hume, D.A., and Pettit, A.R. (2008). Osteal tissue macrophages are intercalated throughout human and mouse bone lining tissues and regulate osteoblast function in vitro and in vivo. J. Immunol. *181*, 1232–1244.

Chow, A., Huggins, M., Ahmed, J., Hashimoto, D., Lucas, D., Kunisaki, Y., Pinho, S., Leboeuf, M., Noizat, C., van Rooijen, N., et al. (2013). CD169$^+$ macrophages provide a niche promoting erythropoiesis under homeostasis and stress. Nat. Med. *19*, 429–436.

Chow, A., Lucas, D., Hidalgo, A., Méndez-Ferrer, S., Hashimoto, D., Scheiermann, C., Battista, M., Leboeuf, M., Prophete, C., van Rooijen, N., et al. (2011). Bone marrow CD169$^+$ macrophages promote the retention of hematopoietic stem and progenitor cells in the mesenchymal stem cell niche. J. Exp. Med. *208*, 261–271.

Cossarizza, A., Chang, H.D., Radbruch, A., Acs, A., Adam, D., Adam-Klages, S., Agace, W.W., Aghaeepour, N., Akdis, M., Allez, M., et al. (2019). Guidelines for the use of flow cytometry and cell sorting in immunological studies (second edition). Eur. J. Immunol. *49*, 1457–1973.

den Haan, J.M., and Kraal, G. (2012). Innate immune functions of macrophage subpopulations in the spleen. J. Innate Immun. *4*, 437–445.

Doyle, L.M., and Wang, M.Z. (2019). Overview of Extracellular Vesicles, Their Origin, Composition, Purpose, and Methods for Exosome Isolation and Analysis. Cells *8*, 727.

Fujiyama, S., Nakahashi-Oda, C., Abe, F., Wang, Y., Sato, K., and Shibuya, A. (2019). Identification and isolation of splenic tissue-resident macrophage subpopulations by flow cytometry. Int. Immunol. *31*, 51–56.

Fukushima, A., Ishida, W., Ojima, A., Kajisako, M., Sumi, T., Yamada, J., Tsuru, E., Miyazaki, J., Tominaga, A., and Yagita, H. (2010). Participation of CD11b and F4/80 molecules in the conjunctival eosinophilia of experimental allergic conjunctivitis. Int. Arch. Allergy Immunol. *151*, 129–136.

Gautier, E.L., Shay, T., Miller, J., Greter, M., Jakubzick, C., Ivanov, S., Helft, J., Chow, A., Elpek, K.G., Gordonov, S., et al.; Immunological Genome Consortium (2012). Gene-expression profiles and transcriptional regulatory pathways that underlie the identity and diversity of mouse tissue macrophages. Nat. Immunol. *13*, 1118–1128.

Ginhoux, F., and Guilliams, M. (2016). Tissue-Resident Macrophage Ontogeny and Homeostasis. Immunity *44*, 439–449.

Grabert, K., Sehgal, A., Irvine, K.M., Wollscheid-Lengeling, E., Ozdemir, D.D., Stables, J., Luke, G.A., Ryan, M.D., Adamson, A., Humphreys, N.E., et al. (2020). A Transgenic Line That Reports CSF1R Protein Expression Provides a Definitive Marker for the Mouse Mononuclear Phagocyte System. J. Immunol. *205*, 3154–3166.

Gray, E.E., Friend, S., Suzuki, K., Phan, T.G., and Cyster, J.G. (2012). Subcapsular sinus macrophage fragmentation and CD169^{+} bleb acquisition by closely associated IL-17-committed innate-like lymphocytes. PLoS ONE *7*, e38258.

Hamann, J., Koning, N., Pouwels, W., Ulfman, L.H., van Eijk, M., Stacey, M., Lin, H.H., Gordon, S., and Kwakkenbos, M.J. (2007). EMR1, the human homolog of F4/80, is an eosinophil-specific receptor. Eur. J. Immunol. *37*, 2797–2802.

Hawley, C.A., Rojo, R., Raper, A., Sauter, K.A., Lisowski, Z.M., Grabert, K., Bain, C.C., Davis, G.M., Louwe, P.A., Ostrowski, M.C., et al. (2018). *Csf1r*-mApple Transgene Expression and Ligand Binding In Vivo Reveal Dynamics of CSF1R Expression within the Mononuclear Phagocyte System. J. Immunol. *200*, 2209–2223.

Hume, D.A., Irvine, K.M., and Pridans, C. (2019). The Mononuclear Phagocyte System: The Relationship between Monocytes and Macrophages. Trends Immunol. *40*, 98–112.

Hur, J., Choi, J.I., Lee, H., Nham, P., Kim, T.W., Chae, C.W., Yun, J.Y., Kang, J.A., Kang, J., Lee, S.E., et al. (2016). CD82/KAI1 Maintains the Dormancy of Long-Term Hematopoietic Stem Cells through Interaction with DARC-Expressing Macrophages. Cell Stem Cell *18*, 508–521.

Idoyaga, J., Suda, N., Suda, K., Park, C.G., and Steinman, R.M. (2009). Antibody to Langerin/CD207 localizes large numbers of CD8alpha^{+} dendritic cells to the marginal zone of mouse spleen. Proc. Natl. Acad. Sci. USA *106*, 1524–1529.

Inman, C.F., Rees, L.E., Barker, E., Haverson, K., Stokes, C.R., and Bailey, M. (2005). Validation of computer-assisted, pixel-based analysis of multiple-colour immunofluorescence histology. J. Immunol. Methods *302*, 156–167.

Jacobsen, R.N., Forristal, C.E., Raggatt, L.J., Nowlan, B., Barbier, V., Kaur, S., van Rooijen, N., Winkler, I.G., Pettit, A.R., and Levesque, J.P. (2014). Mobilization with granulocyte colony-stimulating factor blocks medullar erythropoiesis by depleting F4/80^{+}VCAM1^{+}CD169^{+}ER-HR3^{+}Ly6G^{+} erythroid island macrophages in the mouse. Exp. Hematol. *42*, 547–61.e4.

Karasawa, K., Asano, K., Moriyama, S., Ushiki, M., Monya, M., Iida, M., Kuboki, E., Yagita, H., Uchida, K., Nitta, K., and Tanaka, M. (2015). Vascular-resident CD169-positive monocytes and macrophages control neutrophil accumulation in the kidney with ischemia-reperfusion injury. J. Am. Soc. Nephrol. *26*, 896–906.

Kaur, S., Raggatt, L.J., Millard, S.M., Wu, A.C., Batoon, L., Jacobsen, R.N., Winkler, I.G., MacDonald, K.P., Perkins, A.C., Hume, D.A., et al. (2018). Self-repopulating recipient bone marrow resident macrophages promote long-term hematopoietic stem cell engraftment. Blood *132*, 735–749.

Kaur, S., Sehgal, A., Wu, A.C., Millard, S.M., Batoon, L., Sandrock, C.J., Ferrari-Cestari, M., Levesque, J.P., Hume, D.A., Raggatt, L.J., and Pettit, A.R. (2021). Stable colony-stimulating factor 1 fusion protein treatment increases hematopoietic stem cell pool and enhances their mobilisation in mice. J. Hematol. Oncol. *14*, 3.

Kelm, S., Pelz, A., Schauer, R., Filbin, M.T., Tang, S., de Bellard, M.E., Schnaar, R.L., Mahoney, J.A., Hartnell, A., Bradfield, P., and Crocker, P. (1994). Sialoadhesin, myelin-associated glycoprotein and CD22 define a new family of sialic acid-dependent adhesion molecules of the immunoglobulin superfamily. Curr. Biol. *4*, 965–972.

Kim, M.H., Yang, D., Kim, M., Kim, S.Y., Kim, D., and Kang, S.J. (2017). A late-lineage murine neutrophil precursor population exhibits dynamic changes during demand-adapted granulopoiesis. Sci. Rep. *7*, 39804.

Lewis, S.M., Williams, A., and Eisenbarth, S.C. (2019). Structure and function of the immune system in the spleen. Sci. Immunol. *4*, eaau6085.

Li, W., Wang, Y., Zhao, H., Zhang, H., Xu, Y., Wang, S., Guo, X., Huang, Y., Zhang, S., Han, Y., et al. (2019). Identification and transcriptome analysis of erythroblastic island macrophages. Blood *134*, 480–491.

Liu, Z., Gu, Y., Chakarov, S., Bleriot, C., Kwok, I., Chen, X., Shin, A., Huang, W., Dress, R.J., Dutertre, C.A., et al. (2019). Fate Mapping via Ms4a3-Expression History Traces Monocyte-Derived Cells. Cell *178*, 1509–1525.e19.

Lynch, R.W., Hawley, C.A., Pellicoro, A., Bain, C.C., Iredale, J.P., and Jenkins, S.J. (2018). An efficient method to isolate Kupffer cells eliminating endothelial cell contamination and selective bias. J. Leukoc. Biol. *104*, 579–586.

Macauley, M.S., Crocker, P.R., and Paulson, J.C. (2014). Siglec-mediated regulation of immune cell function in disease. Nat. Rev. Immunol. *14*, 653–666.

Madisen, L., Zwingman, T.A., Sunkin, S.M., Oh, S.W., Zariwala, H.A., Gu, H., Ng, L.L., Palmiter, R.D., Hawrylycz, M.J., Jones, A.R., et al. (2010). A robust and high-throughput Cre reporting and characterization system for the whole mouse brain. Nat. Neurosci. *13*, 133–140.

Mildner, A., Schönheit, J., Giladi, A., David, E., Lara-Astiaso, D., Lorenzo-Vivas, E., Paul, F., Chappell-Maor, L., Priller, J., Leutz, A., et al. (2017). Genomic Characterization of Murine Monocytes Reveals C/EBPβ Transcription Factor Dependence of Ly6C^{-} Cells. Immunity *46*, 849–862.e7.

Misharin, A.V., Morales-Nebreda, L., Mutlu, G.M., Budinger, G.R., and Perlman, H. (2013). Flow cytometric analysis of macrophages and dendritic cell subsets in the mouse lung. Am. J. Respir. Cell Mol. Biol. *49*, 503–510.

Miyake, Y., Asano, K., Kaise, H., Uemura, M., Nakayama, M., and Tanaka, M. (2007). Critical role of macrophages in the marginal zone in the suppression of immune responses to apoptotic cell-associated antigens. J. Clin. Invest. *117*, 2268–2278.

Mossadegh-Keller, N., Sarrazin, S., Kandalla, P.K., Espinosa, L., Stanley, E.R., Nutt, S.L., Moore, J., and Sieweke, M.H. (2013). M-CSF instructs myeloid lineage fate in single haematopoietic stem cells. Nature *497*, 239–243.

Oetke, C., Vinson, M.C., Jones, C., and Crocker, P.R. (2006). Sialoadhesin-deficient mice exhibit subtle changes in B- and T-cell populations and reduced immunoglobulin M levels. Mol. Cell. Biol. *26*, 1549–1557.

Picelli, S., Faridani, O.R., Björklund, A.K., Winberg, G., Sagasser, S., and Sandberg, R. (2014). Full-length RNA-seq from single cells using Smart-seq2. Nat. Protoc. *9*, 171–181.

Ross, I.L., Dunn, T.L., Yue, X., Roy, S., Barnett, C.J., and Hume, D.A. (1994). Comparison of the expression and function of the transcription factor PU.1 (Spi-1 proto-oncogene) between murine macrophages and B lymphocytes. Oncogene *9*, 121–132.

Ross, I.L., Yue, X., Ostrowski, M.C., and Hume, D.A. (1998). Interaction between PU.1 and another Ets family transcription factor promotes macrophage-specific Basal transcription initiation. J. Biol. Chem. *273*, 6662–6669.

Sasmono, R.T., Oceandy, D., Pollard, J.W., Tong, W., Pavli, P., Wainwright, B.J., Ostrowski, M.C., Himes, S.R., and Hume, D.A. (2003). A macrophage colony-stimulating factor receptor-green fluorescent protein transgene is expressed throughout the mononuclear phagocyte system of the mouse. Blood *101*, 1155–1163.

Schindelin, J., Arganda-Carreras, I., Frise, E., Kaynig, V., Longair, M., Pietzsch, T., Preibisch, S., Rueden, C., Saalfeld, S., Schmid, B., et al. (2012). Fiji: an open-source platform for biological-image analysis. Nat. Methods *9*, 676–682.

Schneider, Caroline, A, Rasband, Wayne, S, and Eliceiri, Kevin, W. (2012). NIH Image to ImageJ: 25 years of image analysis. Nature Methods *9* (*7*), 671–675. https://doi.org/10.1038/nmeth.2089.

Seu, K.G., Papoin, J., Fessler, R., Hom, J., Huang, G., Mohandas, N., Blanc, L., and Kalfa, T.A. (2017). Unraveling Macrophage Heterogeneity in Erythroblastic Islands. Front. Immunol. *8*, 1140.

Summers, K.M., and Hume, D.A. (2017). Identification of the macrophage-specific promoter signature in FANTOM5 mouse embryo developmental time course data. J. Leukoc. Biol. *102*, 1081–1092.

Summers, K.M., Bush, S.J., and Hume, D.A. (2020). Network analysis of transcriptomic diversity amongst resident tissue macrophages and dendritic cells in the mouse mononuclear phagocyte system. PLoS Biol. *18*, e3000859.

Sych, T., Mély, Y., and Römer, W. (2018). Lipid self-assembly and lectin-induced reorganization of the plasma membrane. Philos. Trans. R. Soc. Lond. B Biol. Sci. *373*, 20170117.

Tabula Muris Consortium; Overall coordination; Logistical coordination; Organ collection and processing; Library preparation and sequencing; Computational data analysis; Cell type annotation; Writing group; Supplemental text writing group; Principal investigators (2018). Single-cell transcriptomics of 20 mouse organs creates a Tabula Muris. Nature *562*, 367–372.

Tay, J., Bisht, K., McGirr, C., Millard, S.M., Pettit, A.R., Winkler, I.G., and Levesque, J.P. (2020). Imaging flow cytometry reveals that granulocyte colony-stimulating factor treatment causes loss of erythroblastic islands in the mouse bone marrow. Exp. Hematol. *82*, 33–42.

Trapnell, C., Hendrickson, D.G., Sauvageau, M., Goff, L., Rinn, J.L., and Pachter, L. (2013). Differential analysis of gene regulation at transcript resolution with RNA-seq. Nat. Biotechnol. *31*, 46–53.

van Niel, G., D'Angelo, G., and Raposo, G. (2018). Shedding light on the cell biology of extracellular vesicles. Nat. Rev. Mol. Cell Biol. *19*, 213–228.

Winkler, I.G., Sims, N.A., Pettit, A.R., Barbier, V., Nowlan, B., Helwani, F., Poulton, I.J., van Rooijen, N., Alexander, K.A., Raggatt, L.J., and Lévesque, J.P. (2010). Bone marrow macrophages maintain hematopoietic stem cell (HSC) niches and their depletion mobilizes HSCs. Blood *116*, 4815–4828.

Yates, J.L., Racine, R., McBride, K.M., and Winslow, G.M. (2013). T cell-dependent IgM memory B cells generated during bacterial infection are required for IgG responses to antigen challenge. J. Immunol. *191*, 1240–1249.

Yeo, J.H., McAllan, B.M., and Fraser, S.T. (2016). Scanning Electron Microscopy Reveals Two Distinct Classes of Erythroblastic Island Isolated from Adult Mammalian Bone Marrow. Microsc. Microanal. *22*, 368–378.

Yeo, J.H., Lam, Y.W., and Fraser, S.T. (2019). Cellular dynamics of mammalian red blood cell production in the erythroblastic island niche. Biophys. Rev. *11*, 873–894.

Yoshida, Hideyuki, Lareau, Caleb, A, Ramirez, Ricardo, N, Rose, Samuel, A, Maier, Barbara, Wroblewska, Aleksandra, Desland, Fiona, Chudnovskiy, Aleksey, Mortha, Arthur, Dominguez, Claudia, et al. (2019). Thecis-Regulatory Atlas of the Mouse Immune System. Cell *176*, 897–912. https://doi.org/10.1016/j.cell.2018.12.036.

Zhu, Y.P., Padgett, L., Dinh, H.Q., Marcovecchio, P., Blatchley, A., Wu, R., Ehinger, E., Kim, C., Mikulski, Z., Seumois, G., et al. (2018). Identification of an Early Unipotent Neutrophil Progenitor with Pro-tumoral Activity in Mouse and Human Bone Marrow. Cell Rep. *24*, 2329–2341.e8.

STAR★METHODS

KEY RESOURCES TABLE

REAGENT or RESOURCE	SOURCE	IDENTIFIER
Antibodies		
rat anti-mouse/human CD45R/B220-AF594	Biolegend	Cat#103254; RRID:AB_2563229
rat anti-mouse/human CD45R/B220-APCCy7	Biolegend	Cat#103224; RRID:AB_313007
rat anti-mouse/human CD45R/B220-biotin	Biolegend	Cat#103204; RRID:AB_312988
rat anti-mouse/human CD45R/B220-BV785	Biolegend	Cat#103246; RRID:AB_11218795
Rat anti-mouse CD106 (VCAM1)-BUV737	BD Biosciences	Cat#741726; RRID:AB_2871096
Rat anti-mouse CD106 (VCAM1)-Pacblue	Biolegend	Cat#105722; RRID:AB_2304290
Rat anti-mouse CD115-biotin	Biolegend	Cat#135508; RRID:AB_2085223
Rat anti-mouse CD115-BV605	Biolegend	Cat#135517; RRID:AB_2562760
Rat anti-mouse CD117 (cKit)-APC	Biolegend	Cat#105812; RRID:AB_313221
rat anti-mouse/human CD11b-biotin	Biolegend	Cat#101204; RRID:AB_312787
rat anti-mouse/human CD11b-BV510	Biolegend	Cat#101263; RRID:AB_2629529
rat anti-mouse/human CD11b-BV605	Biolegend	Cat#101257; RRID:AB_2565431
rat anti-mouse/human CD11b -PE	Biolegend	Cat#101207; RRID:AB_312790
armenian hamster anti-mouse CD11c-PE	Biolegend	Cat#117308; RRID:AB_313777
armenian hamster anti-mouse CD11c-PerCPCy5.5	Biolegend	Cat#117328; RRID:AB_2129641
rat anti-mouse CD150-PE	Biolegend	Cat#115904; RRID:AB_313683
rat anti-mouse CD150 -APCFire750	Biolegend	Cat#115940; RRID:AB_2629587
rat anti-mouse CD16/CD32	BD Biosciences	Cat#553145; RRID:AB_394660
rat anti-mouse CD169-AF488	Biolegend	Cat#142419; RRID:AB_2566436
rat anti-mouse CD169-PE	Biolegend	Cat#142404; RRID:AB_10915697
rat anti-mouse CD169-PECy7	Biolegend	Cat#142412; RRID:AB_2563911
rat anti-mouse CD3-AF647	Biolegend	Cat#100209; RRID:AB_389323
armenian hamster anti-mouse CD3ε-biotin	Biolegend	Cat#100304; RRID:AB_312669
armenian hamster anti-mouse CD3ε-BV785	Biolegend	Cat#100355; RRID:AB_2565969
armenian hamster anti-mouse CD3ε-PE	Biolegend	Cat#100308; RRID:AB_312673
rat anti-mouse CD4-PECF594	BD Biosciences	Cat#562285; RRID:AB_11154410
rat anti-mouse CD45-APC	Biolegend	Cat#103112; RRID:AB_312977
rat anti-mouse CD45-APCCy7	Biolegend	Cat#103116; RRID:AB_312981
rat anti-mouse CD45-BUV395	BD Biosciences	Cat#564279; RRID:AB_2651134
armenian hamster anti-mouse CD48-BV605	Biolegend	Cat#103441; RRID:AB_2650825
armenian hamster anti-mouse CD48-PerCPCy5.5	Biolegend	Cat#103422; RRID:AB_2075051
rat anti-mouse CD8α-PECF594	BD Biosciences	Cat#562283; RRID:AB_11152075
rat anti-mouse F4/80-AF647	Biolegend	Cat#123122; RRID:AB_893480
rat anti-mouse F4/80-AF647	BD Bioscience	Cat#565853; RRID:AB_2744474
rat anti-mouse F4/80-BV421	BD Bioscience	Cat#565411; RRID:AB_2734779
rat anti-mouse Gr1-biotin	Biolegend	Cat#108404; RRID:AB_313369
rat anti-mouse Ly6B.2-PE	Novus Biologicals	Cat#NBP2-13077PE
rat anti-mouse Ly6C-APCFire750	Biolegend	Cat#128046; RRID:AB_2616731
rat anti-mouse Ly6C-BV785	Biolegend	Cat#128041; RRID:AB_2565852
rat anti-mouse Ly6C-FITC	Biolegend	Cat#128006; RRID:AB_1186135
rat anti-mouse Ly6G-APCFire750	Biolegend	Cat#127652; RRID:AB_2616733
rat anti-mouse Ly6G-BV785	Biolegend	Cat#127645; RRID:AB_2566317
rat anti-mouse Ly6G-PECy7	Biolegend	Cat#127618; RRID:AB_1877261

(*Continued on next page*)

Continued

REAGENT or RESOURCE	SOURCE	IDENTIFIER
rat anti-mouse NKp46-BV711	BD Biosciences	Cat#740822; RRID:AB_2740480
rat anti-mouse Sca1-BUV395	BD Biosciences	Cat#563990; RRID:AB_2738527
rat anti-mouse Sca1-BV510	Biolegend	Cat#108129; RRID:AB_2561593
rat anti-mouse Sca1-BV650	BD Biosciences	Cat#740450; RRID:AB_2740177
rat anti-mouse SiglecF-BV421	BD Biosciences	Cat#562681; RRID:AB_2722581
rat anti-mouse Ter119-APCCy7	Biolegend	Cat#116223; RRID:AB_2137788
rat anti-mouse Ter119-biotin	Biolegend	Cat#116204; RRID:AB_313705
rat anti-mouse Ter119-BUV395	BD Biosciences	Cat#563827; RRID:AB_2738438
rat anti-mouse Ter119-BV785	Biolegend	Cat#116245; RRID:AB_2650921
rat anti-mouse Ter119-FITC	Biolegend	Cat#116206; RRID:AB_313707
rat anti-mouse Ter119-PECy5	Biolegend	Cat#116210; RRID:AB_313711
rat anti-mouse F4/80-None	Abcam	Cat#ab6640; RRID:AB_1140040
goat anti-rat IgG (H+L) Antibody-biotin	Vector Labs	Cat#BA-9401; RRID:AB_2336208
VECTASTAIN Elite ABC-HRP Kit	Vector Labs	Cat#PK-6100; RRID:AB_2336819
Chemicals, peptides, and recombinant proteins		
Streptavidin-APCCy7	Biolegend	Cat#405208
Streptavidin-BV785	BD Biosciences	Cat#405249
Streptavidin-PECF594	BD Biosciences	Cat#562284
Streptavidin-PECy5	Biolegend	Cat#405205
ImmPACT DAB Peroxidase (HRP) Substrate	Vector Labs	Cat#SK-4105
7-AAD (7-Aminoactinomycin D)	Thermofisher	Cat#A1310
Fixable Viability Stain 700	BD Biosciences	Cat#564997
Hoechst 33342	Sigma Aldrich	Cat#B2261
Diphtheria Toxin (DT)	MBL International	Cat# RK-01-517
G-CSF (Filgrastim (Nivestim))	Pfizer Australia	AUST R 160108
Heparin	Pfizer Australia	AUST R 12881
High glucose DMEM	Thermofisher	Cat#11960044
GlutaMAX	Thermofisher	Cat#35050061
Fetal Bovine Serum, qualified, USDA-approved regions	Thermofisher	Cat# 10437028
Tissue-Tek O.C.T Compound	ProSciTech (Sakura)	Cat#IA018
Background Sniper Blocking Reagent	Biocare Medical	Cat# BS966
DaVinci Green Diluent	Biocare Medical	Cat#PD900
Paraformaldehyde, Crystalline	Sigma Aldrich	Cat#P6148
Ethylenediaminetetraacetic acid (EDTA) disodium salt dihydrate	Sigma Aldrich	Cat#E5134
Bovine Serum Albumin, heat shock fraction	Sigma Aldrich	Cat#A7906
4′,6-diamidino-2-phenylindole (DAPI)	Sigma Aldrich	Cat#D9542
TRIzol Reagent	Thermofisher	Cat# 15596018
Critical commercial assays		
CD117 microbeads	Miltenyi Biotech	Cat#130-091-224
RNAeasy mini kit	QIAGEN	Cat#74104
iScript cDNA synthesis kit	BioRad	Cat#1708891
SMARTScribe Reverse Transcriptase	Takara Bio (Clontech)	Cat#639538
RNaseOUT	Thermofisher	Cat#10777-019
Nextera XT DNA sample preparation kit	Illumina	Cat#FC-131- 1096
Nextera XT 24-index kit	Illumina	Cat#FC-131-1001
Taqman Universal Master Mix II	Thermofisher	Cat#4440040

(*Continued on next page*)

Continued

REAGENT or RESOURCE	SOURCE	IDENTIFIER
Taqman Assay - Cd68	Thermofisher	Assay ID - Mm03047343_m1
Taqman Assay - Mertk	Thermofisher	Assay ID - Mm00434920_m1
Taqman Assay - Kit	Thermofisher	Assay ID - Mm00445212_m1
Taqman Assay - Hprt	Thermofisher	Assay ID - Mm00446968_m1
Experimental models: Organisms/strains		
Mouse: C57BL/6J	Australian Resources Centre	RRID:IMSR_JAX:000664
Mouse: *Csf1r*-EGFP	Jackson Laboratory	RRID:IMSR_JAX:018549
Mouse: *Siglec1*$^{\mathrm{Cre}}$	Riken BRC	RRID:IMSR_RBRC06239
Mouse: *Siglec1*$^{\mathrm{DTR}}$	Riken BRC	RRID:IMSR_RBRC04395
Mouse: R26$^{\mathrm{ZsGreen}}$	Jackson Laboratory	RRID:IMSR_JAX:007906
Publicly available datasets		
RNASeq profiles from two distinct F4/80+VCAM1+ sorted bone marrow populations are consistent with non-macrophage cells coated with macrophage fragments	This paper	GSE187052
ImmGen ULI: Systemwide RNA-seq profiles (#1)	(Yoshida et al., 2019)	GSE109125
Gene Expression in sorted myeloid population from mice	This paper	GSE186361
RNASeq on sorted BM myeloid progenitors and monocytes	Mildner et al., 2017	GSE95411
RNASeq on sorted BM macrophages	A-Gonzalez et al., 2017	GSE83222
RNASeq on sorted BM erythroblastic island macrophages	Li et al., 2019	GSE127980
Single Cell RNASeq transcriptomic profiling of murine tissues	Tabula Muris Consortium et al., 2018	https://tabula-muris.ds.czbiohub.org/
Software and algorithms		
FlowJo v10.7.1	TreeStar	https://www.flowjo.com; RRID: SCR_008520
Prism 8.3.1	GraphPad	https://www.graphpad.com; RRID: SCR_002798
Amnis IDEAS Software	Luminex Corp	https://www.luminexcorp.com/imagestreamx-mk-ii/#software
ImageJ	(Schneider et al., 2012)	https://imagej.net/; RRID:SCR_003070
Tophat2	John Hopkins University CCB	http://ccb.jhu.edu/software/tophat/index.shtml; RRID:SCR_013035
Cuffdiff2	Trapnell et al., 2013	http://cole-trapnell-lab.github.io/cufflinks/; RRID:SCR_001647

RESOURCE AVAILABILITY

Lead contact

Further information and requests for resources and reagents should be directed to and will be fulfilled by the lead contact, Allison Pettit (allison.pettit@mater.uq.edu.au).

Materials availability

This study did not generate new unique reagents. Nomenclature summary for marker genes and proteins using in this study is provided in Table S6.

Data and code availability

Data reported in this paper will be shared by the lead contact upon request. RNA-seq data have been deposited at GEO and are publicly available as of the date of publication. Accession numbers for both unique and previously published datasets are detailed in the Key resources table.

- This paper does not report original code.
- Any additional information required to reanalyse the data reported in this paper is available from the lead contact upon request.

EXPERIMENTAL MODEL AND SUBJECT DETAILS

C57BL/6J (wild-type, WT) mice were obtained from Australian Resources Centre (Canning Vale, Western Australia, AU). Transgenic mouse lines were maintained in-house on C57BL/6J strain background; *Csf1r*-EGFP (RRID:IMSR_JAX:018549; (Sasmono et al., 2003)), *Siglec1*^{Cre} (RRID:IMSR_RBRC06239; (Karasawa et al., 2015)) and *Siglec1*^{DTR} (RRID:IMSR_RBRC04395; (Miyake et al., 2007)) sourced from Bio Resource Centre (Yokohama, Kanagawa, Japan), *R26*^{ZsGreen} (RRID:IMSR_JAX:007906; (Madisen et al., 2010)) originally sourced from Jackson Laboratory (Bar Harbor, Maine, USA). Experiments on naive mice were performed on adult mice (< 6mth) of either sex. Animals were maintained under specific pathogen-free conditions in the Translational Research Institute Biological Resource Facility, fed standard chow with *ad libitum* water access and simulated diurnal cycle. Animal experiments were approved by The University of Queensland Health Sciences Ethics Committee and performed in accordance with the Australian Code of Practice for the Care and Use of Animals for Scientific Purposes.

METHOD DETAILS

Macrophage depletion

For macrophage depletion experiments, data and samples from a previously published experiment (Batoon et al., 2019) were reanalysed. In brief, heterozygous adult male *Siglec1*^{DTR} mice (8wk old) were randomly allocated to groups treated with vehicle (0.9% sodium chloride) or 10 μg/kg body weight of diphtheria toxin (DT; MBL International Corporation, MA, USA) once daily via intra-peritoneal injection for up to 4 consecutive days. Tissues were harvested 24 hr after the last injection.

Thioglycollate-elicited macrophages

Female *Csf1r*-EGFP adult mice were treated with two intraperitoneal injections of sterile 4% thioglycollate solution in saline approximately 15 minutes apart. Peritoneal macrophages were collected by saline lavage 5 days after treatment.

Tissue harvesting and processing

Mice were anesthetized and 1 mL blood collected into heparinised tubes by cardiac exsanguination. Femoral BM was collected for flow cytometry by flushing with a 5 mL syringe mounted with 27G needle and 2 × 5 mL of 2% fetal calf serum (FCS) in phosphate buffered saline (PBS). Spleens were dissected and weighed, and a portion of each spleen disaggregated using a either gentle MACS dissociator (Miltenyi Biotec, Cologne, Germany) (Jacobsen et al., 2014) or gently using a 1 mL plunger to push the tissue through a 70 μm strainer. The method of mechanical disruption did not impact the outcome. Lymph nodes (LN) were dissected and gently disaggregated through a 70 μm strainer using a 1 mL plunger. Dissociated cells were filtered through a 40-μm filter prior to antibody staining for flow cytometric analysis. Cell preparations from BM, spleen and LN were stained and analyzed without red-blood-cell (RBC) lysis. Blood was subjected to RBC lysis with 10 volumes lysis buffer (150 mM NH_4Cl, 10 mM $NaHCO_3$, 1 mM EDTA) for 6 min at room temperature prior to washing and resuspension in 2% FCS/PBS for staining. For *in situ* analysis, tissues were fixed using 4% paraformaldehyde. Bones were decalcified using 14% EDTA for at least 2 weeks. Decalcified tissues were processed using a Tissue-Tek VIP 6 Processor (Sakura Finetek, Tokyo, Japan) and paraffin embedded. Spleens were infused with sucrose and cryo-embedded in OCT compound (Sakura Finetek, Tokyo, Japan).

2.4G2 hybridoma supernatant

The 2.4G2 hybridoma produces an antibody that specifically recognizes a common epitope on the extracellular domains of the mouse Fcγ receptors CD16 and CD32, and can be used to block non-antigen-specific binding of immunoglobulins to these receptors. This cell line was sourced in-house, and cultured in high glucose DMEM supplemented with 10% fetal calf serum and 1% GlutaMAX. Supernatant was collected from overgrown cells (not passaged or fed for 2 weeks). Flow cytometric analysis was used to confirm that the supernatant competitively inhibited binding of a PE-conjugated antibody against CD16/CD32.

Flow cytometry

Flow cytometry was performed on BM, spleen, LN, peritoneal lavage and blood single cell suspensions prepared as described above. Cell counts were performed using a BC-5000 Vet Auto Haematology Analyzer (Shenzhen Mindray Bio-Medical Electronics Co) to ensure a consistent number of cells was stained for each sample. When performed, enrichment of c-Kit$^+$ (CD117) cells was achieved using magnetic activated cell sorting (Miltenyi Biotec) as described previously (Barbier et al., 2012). Cells were stained with antibody cocktails (as outlined in gating strategies and detailed in Key resources table), prepared in CD16/CD32 hybridoma 2.4G2 supernatant, for 30 min on ice and then washed with 2% FCS/PBS. Viability dyes (7-amino actinomycin D, Thermofisher, Massachusetts, USA; FVS700, BD Biosciences, New Jersey, USA) were used as per manufacturer's instructions. Flow cytometric analyses were primarily performed using BD Fortessa flow cytometers. Data in Figure 6 was obtained using Cytoflex S and CyAn ADP Analyzers (Beckman Coulter, Brea, CA). Cell sorting was done using BD Aria Fusion sorters (HSPC sorts) or a MoFlo Astrios cell sorter ("macrophage" sorts). Data analysis was performed on singlet events and with dead cells excluded using FlowJo software version 10.7.1 (Tree Star Data Analysis Software; Tree Star, Ashland, OR). T-distributed stochastic neighbor embedding (t-SNE) data dimensionality reduction of the hematopoietic lineage stain was based on the following parameters: FSC, SSC, BV510 (CD11b), BV605 (CD115), BV650 (Sca1), BV785 (Ly6G), PerCPCy5.5 (CD11c), PECF594 (CD4/CD8), APC (Kit) and APCCy7 (B220).

Imaging flow cytometry

Cells were stained with antibody cocktails (as outlined in gating strategies and detailed in Key resources table), prepared in CD16/CD32 hybridoma 2.4G2 supernatant, for 30 min on ice and then washed with 2% FCS/PBS and resuspended at 20 million cells/mL for analysis on a three laser (405nm, 488nm, 642nm) Amnis Imagestream^X MkII Imaging Flow Cytometer (Luminex Corp, Austin, TX). Results were analyzed using Amnis IDEAS Software v6.2.

Immunofluorescent staining and imaging

A Leica CM1950 cryostat (Leica Biosystems, Germany) was used to generate 5 μm sections of decalcified bone and spleen. Sections were stained with antibodies in blocking buffer (PBS containing 5% bovine serum albumin (BSA) and 0.1% Triton X-100) and washed by dipping in PBS. When required, sections were incubated with a PE-CF594 conjugated streptavidin secondary reagent in blocking buffer at room temperature for 1 hour. Sections were washed by dipping in PBS, and where indicated, sections were counterstained with 4′,6-diamidino-2-phenylindole (DAPI). Full antibody details are provided in the Key resources table. Bone sections in Figure 2 were stained with anti-F4/80-AF647 (BD Biosciences). Spleen sections in Figure 4 were stained with anti-B220-biotin (Biolegend), anti-F4/80-BV421 (BD Biosciences), anti-CD169-AF488 (Biolegend) and CD3-AF647 (Biolegend).

BM cell suspension was prepared as for flow cytometry, stained with anti-B220-AF594 (Biolegend) and anti-F4/80-BV421 (BD Biosciences), and cells imaged while in suspension. All imaging was conducted using an Olympus FV3000 confocal laser scanning microscope (Olympus, Tokyo, Japan). For morphometric analysis, digital microscopy images were analyzed using ImageJ software as previously described (Inman et al., 2005). Colocalization analysis was performed using the Coloc 2 ImageJ plugin as described (Schindelin et al., 2012). Briefly, all images were coded and assessed blindly at least 3 sectional depths. Background intensity thresholds were applied using an ImageJ macro which measures pixel intensity across all immunostained and non-stained areas of the images and these were converted to percent staining area.

Immunohistochemical staining

Immunohistochemistry was performed on deparaffinised and rehydrated 4 μm sections as previously described (Batoon et al., 2019), using reagents documented in the Key resources table. Briefly, sections were blocked for endogenous peroxidase activity and subject to antigen retrieval by microwave in 10 mM sodium citrate (pH 6.0). Non-specific antibody binding was blocked using Background Sniper (Biocare Medical). Unconjugated anti-F4/80 was diluted in DaVinci Green Diluent (Biocare Medical) and incubated with sections for 90min. Sections were subsequently washed in Tris-buffered saline, incubated with biotinylated goat anti-rat secondary, washed again, and incubated with Vectastain Elite ABC-HRP, followed by development with ImmPACT DAB Peroxidase Substrate according to manufacturer's instructions. Stained sections were imaged with an Olympus VS120 slide scanner.

Bulk RNA analysis of sorted cell populations

Cells populations for RNA analysis were sorted into 50% FCS/RPMI media. HSPC cell populations were subsequently washed with 2% FCS/PBS and cell pellets snap frozen for RNA extraction using QIAGEN RNAeasy mini kit as per manufacturer's instructions. Reverse transcription (iScript cDNA synthesis kit) was performed prior to qPCR analysis with Taqman gene expression assays (see Key resources table). Assay reactions were run in Taqman Universal Master Mix II on a ViiA 7 Real-Time PCR System, and analyzed with QuantStudio Real-Time PCR Software. RNA extraction from cell populations sorted by positive selection for macrophage markers was performed using Trizol reagent, followed by column clean-up using QIAGEN RNAeasy mini kit. The cDNA libraries for sequencing were generated as described previously (Bisht et al., 2019). The reverse transcription mastermix was prepared according to Picelli et al.(2014) with the following modifications. SMARTScribe Reverse Transcriptase was used in place of SuperScript II, and the RNase inhibitor used was RNaseOUT. The template switching oligo did not contain any locked nucleic acids but was modified with biotin to prevent concatemerization. PCR pre-amplification was performed using 18 cycles. The amplicons were cleaned using Ampure beads as previously described (Picelli et al., 2014), and tagmented using the Nextera XT DNA sample preparation kit. Libraries were barcoded with Illumina adaptors from the Nextera XT 24-index kit and amplified with 13 cycles of PCR. Final libraries were subject to equimolar pooling at 2.5 nM. Libraries were gel purified to select for 200-600bp fragments and sequenced on an Illumina NextSeq500 instrument using the high output kit in the 75 bp paired-end configuration. Reads were mapped to the mouse genome (mm9) using Tophat2 with default parameters. Transcript abundance was computed with Cuffdiff2 (Trapnell et al., 2013). The MyGeneset databrowser (https://www.immgen.org/Databrowser19/DatabrowserPage.html) was used to compare transcript levels of the top 200 most abundant genes within each "macrophage" population across the ImmGen ULI-RNA-Seq datasets (GEO: GSE127267).

QUANTIFICATION AND STATISTICAL ANALYSIS

Graphing and statistical analyses were conducted using GraphPad Prism 8.3.1. Imaging flow cytometric stain area data was assessed using non-parametric tests (eg Kruskal Wallis), whereas all other data (flow cytometric population frequency data, gene expression) were assessed by parametric tests. Where statistical analysis involved multiple comparisons, a multiple comparison correction was applied according to the software recommendation. All sample sizes and statistical tests employed are documented in figure legends.